Monthly Notices
of the
ROYAL ASTRONOMICAL SOCIETY

MNRAS **471,** 629–649 (2017)
Advance Access publication 2017 June 22

doi:10.1093/mnras/stx1569

Boötes-HiZELS: an optical to near-infrared survey of emission-line galaxies at $z = 0.4$–4.7

Jorryt Matthee,[1]★ David Sobral,[2,1] Philip Best,[3] Ian Smail,[4] Fuyan Bian,[5]† Behnam Darvish,[6] Huub Röttgering[1] and Xiaohui Fan[7]

[1]*Leiden Observatory, Leiden University, PO Box 9513, NL-2300 RA Leiden, the Netherlands*
[2]*Department of Physics, Lancaster University, Lancaster LA1 4YB, UK*
[3]*Institute for Astronomy, University of Edinburgh, Royal Observatory, Blackford Hill, Edinburgh EH9 3HJ, UK*
[4]*Centre for Extragalactic Astronomy, Department of Physics, Durham University, South Road, Durham DH1 3LE, UK*
[5]*Research School of Astronomy & Astrophysics, Mt Stromlo Observatory, Australian National University, Weston Creek, ACT 2611, Australia*
[6]*Cahill Center for Astrophysics, California Institute of Technology, 1216 East California Boulevard, Pasadena, CA 91125, USA*
[7]*Steward Observatory, University of Arizona, 933 North Cherry Avenue, Tucson, AZ 85721, USA*

Accepted 2017 June 20. Received 2017 June 16; in original form 2017 February 12

ABSTRACT

We present a sample of ∼1000 emission-line galaxies at $z = 0.4$–4.7 from the ∼0.7deg^2 High-z Emission-Line Survey in the Boötes field identified with a suite of six narrow-band filters at ≈0.4–2.1 μm. These galaxies have been selected on their Ly α (73), [O II] (285), H β/[O III] (387) or H α (362) emission line, and have been classified with optical to near-infrared colours. A subsample of 98 sources have reliable redshifts from multiple narrow-band (e.g. [O II]–H α) detections and/or spectroscopy. In this survey paper, we present the observations, selection and catalogues of emitters. We measure number densities of Ly α, [O II], H β/[O III] and H α and confirm strong luminosity evolution in star-forming galaxies from $z \sim 0.4$ to ∼5, in agreement with previous results. To demonstrate the usefulness of dual-line emitters, we use the sample of dual [O II]–H α emitters to measure the observed [O II]/H α ratio at $z = 1.47$. The observed [O II]/H α ratio increases significantly from 0.40 ± 0.01 at $z = 0.1$ to 0.52 ± 0.05 at $z = 1.47$, which we attribute to either decreasing dust attenuation with redshift, or due to a bias in the (typically) fibre measurements in the local Universe that only measure the central kpc regions. At the bright end, we find that both the H α and Ly α number densities at $z \approx 2.2$ deviate significantly from a Schechter form, following a power law. We show that this is driven entirely by an increasing X-ray/active galactic nucleus fraction with line luminosity, which reaches ≈100 per cent at line luminosities $L \gtrsim 3 \times 10^{44}$ erg s^{-1}.

Key words: galaxies: active – galaxies: evolution – galaxies: high-redshift – galaxies: luminosity function, mass function – galaxies: star formation.

1 INTRODUCTION

Understanding how and when galaxies grow their stellar mass and in some cases eventually stop forming stars are key goals of galaxy formation theory. However, since it is only possible to observe an individual galaxy at a single epoch, to assess their evolution it is crucial to homogeneously select equivalent samples of galaxies over a wide redshift range. Currently, different epochs in cosmic time are probed by different selections of galaxies. Moreover, the galaxy properties (such as star formation rates and estimates of dust attenuation) are measured with different tracers (e.g. Speagle et al. 2014). Therefore, it is important to understand whether local calibrations can be extrapolated to high redshift. This requires large samples of galaxies with a well understood selection function and a large dynamic range in galaxy properties.

Homogeneously selected samples of star-forming galaxies can be obtained with narrow-band (NB) surveys that are very efficient in selecting emission-line galaxies. Using different NBs, galaxies can be selected on a particular emission line across a range of redshifts with well-defined line-luminosity and equivalent width (EW) limits. For example, in specific windows from the optical to the near-infrared, ground-based NB surveys can select H $\alpha_{\lambda 6563}$ emission-line galaxies up to $z \sim 2.6$ (e.g. Bunker et al. 1995; Malkan, Teplitz & McLean 1996; van der Werf, Moorwood & Bremer 2000;

★ E-mail: matthee@strw.leidenuniv.nl
† Stromlo fellow.

Ly et al. 2007; Geach et al. 2008; Tadaki et al. 2011; Lee et al. 2012; Drake et al. 2013; Sobral et al. 2013, 2015; Stroe & Sobral 2015). The Hα recombination-line is a reliable tracer of star-formation rate on >10 Myr time-scales (Kennicutt 1998) and is less sensitive to attenuation due to dust than other shorter wavelength tracers (e.g. Garn et al. 2010; Ibar et al. 2013; Stott et al. 2013). At redshifts $z > 2.5$, the most commonly used rest-optical emission lines are challenging to observe (but see e.g. Khostovan et al. 2015), while the rest-frame UV Lyman-$\alpha_{\lambda 1216}$ (Lyα) line, intrinsically the strongest emission line emitted in H II regions is efficiently observed up to $z \sim 7$ (e.g. Rhoads et al. 2000; Dawson et al. 2007; Ouchi et al. 2008; Lee et al. 2014; Matthee et al. 2015; Santos, Sobral & Matthee 2016), but is extremely sensitive to resonant scattering and dust attenuation (e.g. Hayes 2015).

Our High-z Emission-Line Survey (HiZELS; Geach et al. 2008; Best et al. 2013; Sobral et al. 2013) has been designed to observe multiple emission lines in different NBs simultaneously. Hence, Sobral et al. (2012) used observations with NB921 at ≈920 nm and NB_H at ≈1620 nm to jointly observe [O II]$_{\lambda\lambda 3726, 3729}$ and Hα at $z = 1.47$. At $z = 2.2$, matched NB surveys have observed (combinations of) Lyα+[O II]+[O III]$_{\lambda\lambda 4959, 5007}$+H$\alpha$ at $z = 2.2$ (Lee et al. 2012; Nakajima et al. 2012; Oteo et al. 2015; Matthee et al. 2016; Sobral et al. 2017). One of the advantages of this dual (or multiple) NB technique is that identification of the specific emission line is secure, such that dual-emitters may be used to fine-tune colour selection criteria (in particular in fields where only limited multiwavelength data are available). Another advantage is that various star formation rate (SFR) estimators, for example [O II] or (to lesser extent) Lyα, can be calibrated with joint Hα observations.

Here, we present the first results from Boötes-HiZELS, which is a survey of a central 0.7 deg^2 region in the Boötes field with a suite of six narrow-band filters, split into two sets: three red filters at ≈921, 1620 and 2120 nm from HiZELS that select rest-optical lines such as Hα,[1] Hβ/[O III][2] and [O II], complemented by three blue filters at ≈392, 411 and 501 nm that select Lyα emitters (LAEs). Using these narrow-band filters, we select samples of emission-line galaxies using their Hα line at $z = 0.4$–2.2 and $z = 0.8$–4.7 with Hβ/[O III], [O II] and Lyα. These samples are used as targets for ongoing detailed spectroscopic follow-up studies.

This paper presents the selection and classification of line-emitters, their global properties such as number densities, the number of dual-NB emitters and X-ray detections. We compare our number densities to published luminosity functions (LFs) for samples in the range $z \approx 0.4$–4.7 and we study [O II]–Hα emitters at $z = 1.47$. These emitters can be used to measure whether the observed [O II]/Hα ratio changes with redshift (e.g. Hayashi et al. 2013), which is essential for studies employing [O II] as a SFR indicator at $z > 1$ (e.g. Ly et al. 2012). We also use the available deep X-ray coverage to study the X-ray fractions of line-emitters.

We present the observations and archival data used in this survey in Section 2. The data reduction, characteristics and catalogue production and selection of emitters are presented in Section 3. Section 4 presents our procedure for classifying emission-line galaxies. We present the number densities of classed line-emitters and compare these to published LFs in Section 5. In Section 6, we investigate the properties of dual-NB line-emitters, the observed [O II]/Hα ratio at $z = 1.47$ and the X-ray fractions of Hα emitters (HAEs) and LAEs. Finally, Section 7 presents our conclusions.

We adopt a Λ cold dark matter (ΛCDM) cosmology with $H_0 = 70$ km s^{-1}Mpc^{-1}, $\Omega_M = 0.3$ and $\Omega_\Lambda = 0.7$. Magnitudes are in the AB system measured in 3 arcsec apertures, unless noted otherwise.

2 OBSERVATIONS AND DATA

We observed a 0.7 deg^2 region in the Boötes field with six narrow-band filters (NB392, stV, NB501, NB921, NB_H and NB_K). The Boötes field was chosen for the availability of deep multiwavelength data (see e.g. Lee et al. 2011; Bian et al. 2012, 2013; Beare et al. 2015) over a relatively large area, avoiding the galactic plane and its observability from La Palma and Hawaii. In addition to publicly available broad-band (BB) imaging in the *U*, *B*, *R*, *I*, *J* and *K* bands (described in Section 2.1), we also obtain the missing wavelength coverage with three broad-band filters *g*, *z* and *H* (see Table 1 for an overview).

2.1 Public/archival multiwavelength data

The Boötes field has been imaged in the optical by the NOAO Deep Wide Field survey[3] in *Bw*, *R* and *I* (Jannuzi & Dey 1999) and by the LBT Bootes Field Survey in the *U* and *Y* bands (Bian et al. 2013). Near-infrared data in the *J*, *H* and *Ks* band are available from the Infrared Bootes Imaging Survey (Gonzalez et al. 2010), although we do not use the *H*-band data as our data are deeper. The general characteristics of the archival data used in this paper are listed in Table 1. In addition, the field has been imaged in the X-ray by *Chandra* (Murray et al. 2005), in the UV by the *GALEX* Deep Imaging Survey (Martin et al. 2005), in the mid-infrared by *Spitzer*/IRAC (Ashby et al. 2009) and in the far-infrared by *Herschel* as part of the *Herschel* Multi-tiered Extragalactic Survey (Oliver et al. 2012). However, the X-ray, UV and mid- and far-infrared data are not explicitly used in the selection of line-emitters. In addition, Williams et al. (2016) presented deep low-frequency (150 MHz) radio observations in this field. Finally, spectroscopic follow-up of mostly X-ray-selected sources [and hence active galactic nucleus (AGN)] has been performed by Kochanek et al. (2012).

2.2 Optical observations

Optical observations in two narrow-band filters (NB392, NB501), a medium band filter (stV) and the *g* band were performed with the Wide Field Camera (WFC) on the 2.5-m Isaac Newton Telescope, part of the Roque de los Muchachos Observatory on the island of La Palma, Spain. WFC has a mosaic of four CCDs with a combined field of view of 0.3 deg^2 and a 0.33 arcsec pixel scale (see Table 1). The survey was designed with four pointings, each with a

[1] We note that narrow-band Hα measurements measure the line-flux and EW of the combined Hα and [N II] doublet depending on the precise redshift. Therefore, a correction needs to be applied to measure Hα EWs and line-fluxes. For simplicity, we refer to Hα + [N II] emitters as Hα emitters from now on.

[2] Typical photometric redshifts are not accurate enough to distinguish between Hβ line-emitters and a line-emitter with one of the [O III] lines. Moreover, depending on the specific redshift, we either detect Hβ, or one or two of the [O III] lines in the narrow-band filter. The majority of Hβ/[O III] emitters are [O III]$_{\lambda 5007}$ emitters, as this line is typically the stronger line [see Sobral et al. (2015) and Khostovan et al. (2015) for details]. Yet, to remind the reader of these caveats, we call these emitters Hβ/[O III] emitters throughout the paper.

[3] http://noao.edu/noao/noaodeep/

Table 1. Description of the available (archival and new) multiwavelength data in Boötes-HiZELS, with narrow-band filters highlighted in bold. The abbreviations for the archival surveys are: LBFS – LBT Boötes Field Survey (Bian et al. 2013); NDWFS – NOAO Deep Wide Field Survey (Jannuzi & Dey 1999); IBIS – Infrared Bootes Imaging Survey (Gonzalez et al. 2010). λ_c is the central wavelength of the filter and $\Delta\lambda$ is the width between the full width half-maxima of the filter transmission. The full width half-maximum (FWHM) of the point spread function has been measured as described in Section 2.2. We list the total exposure time per pixel and its variance. For NB921 and *z*, 60 per cent of the coverage has the highest exposure time listed. Depths are measured by measuring the sky value in 100 000 3 arcsec apertures on blank regions in the images as described in Section 3.2.2. The coverage is after masking each individual filter for uncovered regions or regions with insufficient depth.

Filter	Telescope	Survey	λ_c (nm)	$\Delta\lambda$ (nm)	FWHM (arcsec)	Exposure time (ks)	Dates	Depth (3σ, AB)	Coverage (deg^2)
U	LBT	LBFS	359	54	1.2			25.3	0.78
NB392	INT	This survey	392	5.2	1.8	12.4 ± 2.0	2013 June 6–10; 2014 February 27, March 1–8, 27	24.3	0.54
B_w	Mayall	NDWFS	464	110	1.4			25.4	0.78
stV	INT	This survey	410	16	1.9	3.8 ± 0.8	2013 June 6–10; 2014 March 2, 5–7; 2016 June 11–13	24.1	0.63
g	INT	This survey	485	129	1.6	6.0 ± 0.0	2016 June 6–8	24.9	0.78
NB501	INT	This survey	501	10	1.6	8.4 ± 0.1	2015 April 11, 12, 16, 17; 2016 June 5–7, 10, 12	24.7	0.74
R	Mayall	NDWFS	602	160	1.1			25.0	0.78
I	Mayall	NDWFS	754	170	1.1			24.4	0.78
z	Subaru	This survey	878	113	0.8	1.0–2.1	2014 May 28, 29	24.3	0.76
NB921	Subaru	This survey	919	13	0.8	2.16–2.52	2014 May 28, 29	24.0	0.46
Y	LBT	LBFS	984	42	0.8			23.1	0.78
J	NEWFIRM	IBIS	1300	190	1.0			22.9	0.78
H	UKIRT	This survey	1600	200	0.8	1.2 ± 0.1	2010 April 2–8	22.6	0.78
NB$_H$	UKIRT	This survey	1620	21	0.8	15.4 ± 1.4	2010 April 2–6	22.1	0.74
K	NEWFIRM	IBIS	2260	280	1.2			22.1	0.78
NB$_K$	UKIRT	This survey	2120	21	1.2	20.2 ± 0.0	2010 April 8, 9, 14, July 18–23; 2011 February 16, 27, 28, March 9, 12, 16, 20, 22–26	22.3	0.73

C-NE-NW-SE-SW dither pattern (with 30 arcsec offsets). Individual exposure times for narrow and medium-bands were either 0.2 or 1.0 ks, depending on whether the telescope could successfully guide on a star (since the auto-guider CCD is behind the filter, this is challenging for narrow-band filters in extragalactic fields) and the stability of the weather. The individual exposure times for the *g* band were 0.6 ks.

Observations in the NB921 narrow-band filter and the *z* filter were performed with Suprime-Cam (S-cam) on the 8.0-m Subaru telescope of the National Astronomical Observatory of Japan. S-cam consists of a mosaic of 10 CCDs with a combined field of view of 0.255 deg^2 with a 0.2-arcsec pixel scale. We imaged the field with the *z* (NB921) filter with five (three) pointings. For NB921, we used individual 360-s exposures dithered either seven (two pointings) or six (one pointing) times. For *z*, we used individual 150-s exposures of the same pointings as NB921 dithered 14 times, and 3 times 100-s exposures in the other two pointings. Observations were done sequentially to avoid contamination of the emission-line sample by variable sources and/or supernova (i.e. Matthee et al. 2014).

2.3 Near-infrared observations

Near-infrared observations in *H*, NB$_H$ and NB$_K$ were performed with WFCAM on the UK Infrared Telescope (UKIRT) on Mauna Kea as part of the HiZELS (e.g. Sobral et al. 2013). WFCAM has a 'paw-print' configuration of four CCDs, with a total field of view of 0.21 deg^2 and a 0.4- arcsec pixel scale. The field was imaged with four pointings in a dither sequence of 14 exposures with small offsets. Due to the high sky background in the near-infrared, the individual exposure times were 10 s, 100 s and 60 s for *H*, NB$_H$ and NB$_K$, respectively, to avoid saturation. In order to obtain the final depth, this dither sequence was typically repeated 9, 11 and 24 times for the respective filters.

3 DATA REDUCTION AND CATALOGUE PRODUCTION

3.1 Data reduction

3.1.1 Optical

We reduce data from the INT/WFC with a custom-made pipeline based on PYTHON described in detail in Stroe et al. (2014) and Sobral et al. (2017) and we reduce Subaru/S-Cam data similarly with SDFRED2 (Ouchi et al. 2004). In summary, we first bias subtract individual frames using a master bias from the median stack of bias frames for the corresponding night. We then create a master flat by median combining twilight flats and use it to flat-field the individual frames. Subsequently, we measure the full width half-maximum (FWHM) of the point spread function (PSF) using unsaturated stars in individually reduced frames with SExtractor (Bertin & Arnouts 1996), and reject frames with PSF FWHM above the chosen target FWHM listed in Table 1. This is particularly important for some exposures with the INT/WFC that have been observed in poor conditions. We then match the PSF of remaining frames before combining frames to the common mosaic by smoothing the images with a Gaussian kernel.

3.1.2 Near-infrared

Near-infrared data from UKIRT/WFCAM have been reduced using PfHiZELS [see Sobral et al. (2009) and Sobral et al. (2013) for

full details]. The steps are similar to the steps in the optical data reduction, except for dark subtraction instead of bias subtraction and the master flat that is based on an iterative self-flat method using the science frames themselves, instead of relying on twilight flats (see Sobral et al. 2013).

3.1.3 Astrometric alignment

The reduced frames are astrometrically registered to the 2-Micron All-Sky Survey (2MASS) point source catalogue (Skrutskie et al. 2006) with SCAMP (Bertin 2006). Frames are then co-added, resampled to a pixel scale of 0.33 arcsec and mapped to the MOSAIC pointing with SWARP (Bertin 2010). We apply the same method for public data described in Section 2.1.

While extracting initial catalogues, we encountered significant astrometric distortions of up to 1.2 arcsec in the edges of the cameras of the public B_w, R and I data. These distortions significantly affect dual-mode photometry (described in Section 3.2.1). In order to obtain a more accurate astrometric solution for these data, we used the SCAMP software to remap the images to the SDSS DR7 astrometry (Abazajian et al. 2009). The astrometric differences between 2MASS and SDSS are minimal and no significant distortions affecting our photometry have been noticed after this correction.

3.1.4 Photometric calibration

We set the photometric zero-point (ZP) of the images to an arbitrary common ZP = 30 by matching the MAG-AUTO photometry in the combined images to the following available data: g and z are calibrated to SDSS and H and K to 2MASS. We then use the broad-bands available to calibrate the narrow-bands in the two following steps: we first calibrated NB921 to z, NB_H and NB_K are calibrated to H and K, NB501 to g from SDSS, and NB392 and stV to B_w. After this first step, we have to correct for the fact that most narrow-band central wavelengths are not in the centre wavelength of the broad-band filters, which leads to a bias in line-flux measurements due to gradients in the continuum. This can be resolved by using colour information in adjacent broad-bands. For NB921, NB_H and NB_K, we follow the corrections described in Sobral et al. (2013) and for NB392 we use the corrections from Matthee et al. (2016). We derive the following correction for stV: $stV_{cor} = stV - 0.23(U - B_w) + 0.24$. For sources undetected in U and B_w, we apply the median correction of +0.04. We do not apply a correction for NB501, as it is close to the centre of the g band.

3.2 Catalogue production

3.2.1 Photometry

Photometry of the optical-NIR filters listed in Table 1 is performed with SEXTRACTOR in dual-image mode. We create six catalogues, each with one of the six narrow-bands as detection image. Photometry is measured within circular apertures with a diameter of 3 arcsec. For each narrow-band, we measure the narrow-band and the corresponding broad-band magnitudes from images with their PSF matched to the narrow-band imaging. We also measure the magnitudes in all broad-bands with their PSF matched to the g-band PSF (1.6 arcsec FWHM). The measurements with the PSF from the NB are used to select line-emitters and compute emission-line properties such as line-flux and EW. The other measurements are used for colour–colour selections.

We have produced a mask for each narrow-band individually, where we mask regions around bright, saturated stars, CCD bleeding, cross-talk in near-infrared detectors and regions with low signal-to-noise ratio (S/N) or incomplete coverage (e.g. Sobral et al. 2009; Santos et al. 2016).

3.2.2 Depths

We estimate the depth of images by measuring the standard deviation of the total counts in 100 000 apertures with a diameter of 3 arcsec placed at random (but avoiding sources) locations in our images. 3σ depths range from ∼25 AB magnitude in blue broad-band filters to ∼22 AB magnitude in the near-infrared filters (see Table 1).

3.3 Selecting line-emitters

Line-emitters are selected based on two criteria: the narrow-band excess (the EW) must be high enough and the excess must be significant. For the narrow-band filters NB392, stV, NB501, NB921, NB_H and NB_K, we use the corresponding broad-band filters U, B_w, g, z, H and K. In order to convert the photometric narrow-band excess to observed EW, we convert magnitudes (m_i) to flux densities in each filter (f_i) with the standard AB magnitude convention:

$$f_i = \frac{c}{\lambda_{i,\mathrm{centre}}^2} 10^{-0.4(m_i+48.6)}, \quad (1)$$

where c is the speed of light and $\lambda_{i,\mathrm{centre}}$ is the central wavelength in each filter. Next, we use the following equations to convert the narrow-band and their corresponding broad-bands to EW:

$$\mathrm{EW_{obs}} = \Delta\lambda_{\mathrm{NB}} \frac{f_{\mathrm{NB}} - f_{\mathrm{BB}}}{f_{\mathrm{BB}} - f_{\mathrm{NB}} \frac{\Delta\lambda_{\mathrm{NB}}}{\Delta\lambda_{\mathrm{BB}}}}. \quad (2)$$

Here, f_{NB} and f_{BB} are the flux densities in the narrow-band and broad-band and $\Delta\lambda_{\mathrm{NB}}$ and $\Delta\lambda_{\mathrm{BB}}$ the filter widths. In equation (2), the numerator is the difference in narrow-band and broad-band flux and the denominator is the continuum level, corrected for the contribution from the flux in the narrow-band. For sources without broad-band detection, we set the EW to a lower limit. This lower limit ranges from 550 Å for NB392 and NB501 to 2500 Å for stV depending on the width of the NB filter and the depth of the BB data used to measure the continuum. The lower limit is around ≈1200 Å for near-infrared NBs.

The excess significance (Σ) quantifies whether a certain narrow-band excess is due to errors in the narrow-band and broad-band photometry or not. Hence, we follow the methodology presented in Bunker et al. (1995) and the equation from Sobral et al. (2013) to compute Σ:

$$\Sigma = \frac{1 - 10^{-0.4(\mathrm{BB-NB})}}{10^{-0.4(\mathrm{ZP-NB})} \sqrt{(\sigma_{\mathrm{box,BB}}^2 + \sigma_{\mathrm{box,NB}}^2)}}, \quad (3)$$

where BB is the broad-band magnitude used for the continuum estimate, NB is the narrow-band magnitude and ZP is the zero-point of the images. σ_{box} is the root mean squared (rms) of background aperture values in the data of the respective filters (see Section 3.2.2).

The line-flux is computed using

$$f_{\mathrm{line}} = \Delta\lambda_{\mathrm{NB}} \frac{f_{\mathrm{NB}} - f_{\mathrm{BB}}}{1 - \frac{\Delta\lambda_{\mathrm{NB}}}{\Delta\lambda_{\mathrm{BB}}}}. \quad (4)$$

We select line-emitters amongst narrow-band selected sources in all six narrow-band filters with the criterion that $\Sigma > 3$. However,

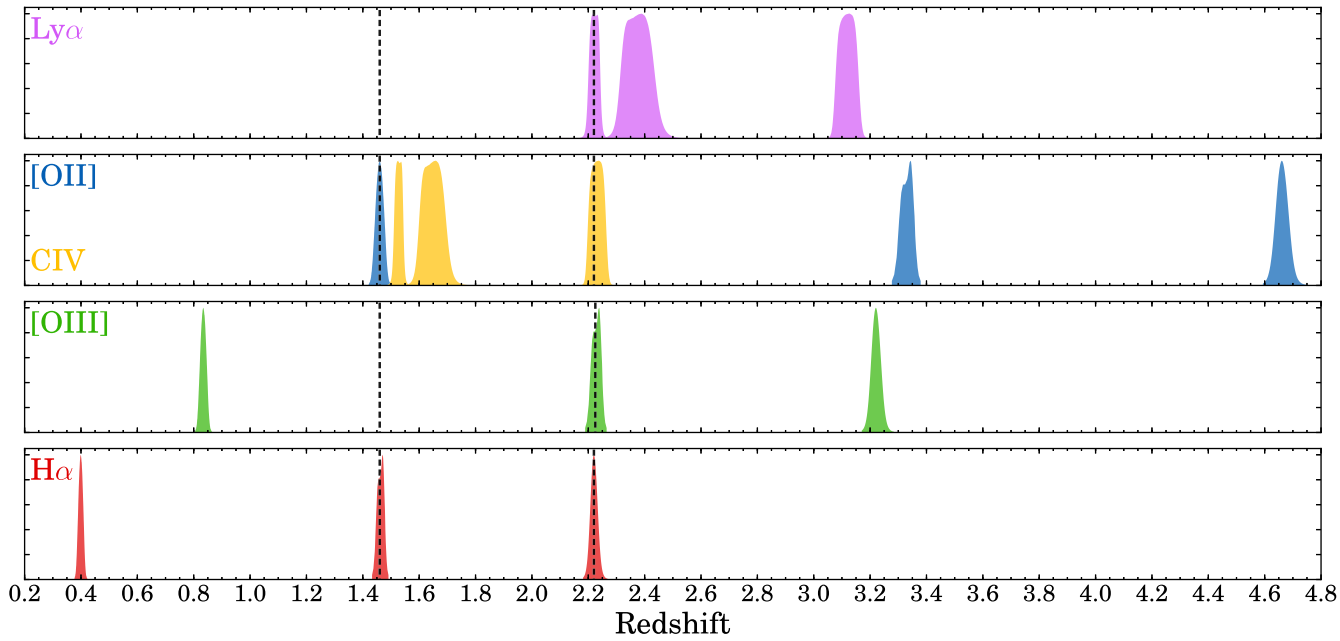

Figure 1. Redshift slices for different emission lines probed by our Boötes-HiZELS survey. As highlighted by the dashed lines, there is joint coverage of [O II] and H α at $z = 1.47$ and of Ly α, [O III] and H α at $z = 2.22$. By coincidence, there is also matched volume coverage of C IV at this redshift.

because each narrow-band has different filter characteristics, we do not apply a homogeneous excess (EW) selection threshold. For each filter, we apply the criterion that the observed EW is three times the standard scatter in observed EWs for sources detected at $>15\sigma$. This means that we apply EW $>$30, 130, 50, 30, 85, 80 Å for NB392, stV, NB501, NB921, NB_H and NB_K, respectively.

Before obtaining our final list of line-emitters, in each filter, we visually inspect all the sources in the narrow-band images for remaining spurious sources such as artefacts from bright stars, cosmic rays or misidentifications by SExtractor. This can happen when the noise properties vary strongly locally, which is the case in small regions of the coverage by the NB392, stV and NB921 filters.

4 CLASSIFYING LINE-EMITTERS

Fig. 1 shows the redshift ranges where our narrow-band filters sample the brightest emission lines seen in normal star-forming galaxies and AGN. By a combination of design and coincidence, the HiZELS narrow-band filters coincide with several different emission lines at specific redshifts. At $z = 1.47$, the NB921/NB_H combination is sensitive to the [O II] and H α lines (Sobral et al. 2012). At $z = 2.23$, the Ly α, [O III] and H α lines fall in the NB392/NB_H/NB_K combination.[4] At $z = 2.23$, the NB501 filter is also sensitive to C IV emission. The redshifts of line-emitters detected in several narrow-bands (dual-emitters) can be estimated accurately and we refer to them as z_{dualNB} in the remainder of this paper. As can be seen in Table C1, dual-emitters are found as faint as $I \approx 25$, three magnitudes fainter than typical available spectroscopic redshifts, which were mostly for X-ray-selected sources.

Line-emitters that have no existing spectrosopic redshift or are not detected as dual-emitters are classified using colour–colour selections tuned to identify Lyman and Balmer breaks at various redshift intervals. For the blue narrow-bands, we use colour selections to identify Ly α emitters. For the red filters, we use colour selections to identify H α emitters, H β/[O III] emitters and [O II] emitters (see also similar selections in Sobral et al. 2013; Khostovan et al. 2015).

The main strategy to devise colour criteria has been as follows: after removing stars (due to atmospheric features in the blue or the near-infrared, stars may be picked up with a narrow-band excess) using their *uJK* colours (e.g. Muzzin et al. 2013), we start with colour selections from the literature, which we slightly modify using the spectroscopically confirmed line-emitters and the dual-emitters. Colour criteria are stated explicitly below and listed in Table 3. We summarize the number of emitters and classified line-emitters in Table 4.

4.1 Line-emitters in NB392

The narrow-band NB392 has specifically been designed to conduct a Ly α survey with a matched volume coverage to H α emitters identified with the HiZELS NB_K filter (H_2S1) at $z = 2.23$ in order to study the Ly α escape fraction and its dependencies on galaxy properties, as described in detail in Matthee et al. (2016) and Sobral et al. (2017).

We select 57 line-emitters with an excess criterion of $EW_{obs} > 30$ Å (U-NB392 $>$0.45). For LAEs at $z = 2.23$, this corresponds to $EW_0 > 9$ Å (it is possible to go to such low EWs because the width of NB392 is very narrow). Although Ly α surveys at $z \approx 2$–3 typically invoke a higher EW criterion of $\sim$25–30 Å (e.g. Ouchi et al. 2008; Nakajima et al. 2012), we found that such a selection results in missing the most luminous LAEs at $z = 2.2$ in the COSMOS and Ultra Deep Survey (UDS) fields (Sobral et al. 2017). This is because these sources are typically AGN, which have bright Ly α emission on the top of a bright UV continuum.

Using the spectroscopy available from AGES (Kochanek et al. 2012), we find eight Mg II emitters at $z = 0.4$ and five line-emitters at $z > 1$ (including two LAEs at $z = 2.2$) (see Table 2). By matching the sample of line-emitters with the samples of line-emitters in NB_H and NB_K (see below), we add four other robust

[4] In this case, it is certain that the emission line in NB_H is [O III] and not H β.

Table 2. Spectroscopically and dual-NB confirmed emission lines observed in narrow-band filters. We note that spectroscopic redshifts are highly biased towards AGN and that the spectroscopic redshift distribution does not resemble the real redshift distribution, particularly for fainter line-emitters. Dual-NB redshifts are only available at $z = 1.47$ and $z = 2.23$ (see Fig. 1).

Filter	Emission line	Redshift	# $z_{\rm spec}$	# $z_{\rm dual-NB}$
NB392	Mg II$_{\lambda2798}$	0.39–0.41	8	–
	C III]$_{\lambda1909}$	1.04–1.07	1	–
	C IV$_{\lambda1549}$	1.51–1.55	2	–
	Ly $\alpha_{\lambda1216}$	2.20–2.24	2	5
stV	Mg II$_{\lambda2798}$	0.42–0.50	1	–
	C III]$_{\lambda1909}$	1.10–1.20	3	–
	He II$_{\lambda1640}$	1.44–1.56	1	–
	C IV$_{\lambda1549}$	1.59–1.71	4	–
	Ly $\alpha_{\lambda1216}$	2.30–2.45	6	–
NB501	[O II]$_{\lambda3727}$	0.32–0.36	1	–
	Mg II$_{\lambda2798}$	0.76–0.81	1	–
	C IV$_{\lambda1549}$	2.19–2.27	1	3
	Ly $\alpha_{\lambda1216}$	3.06–3.17	5	–
NB921	H $\alpha_{\lambda6563}$	0.39–0.41	5	–
	[O III]$_{\lambda\lambda4959,\,5007}$	0.82–0.87	1	–
	[O II]$_{\lambda3727}$	1.44–1.48	0	20
	Mg II$_{\lambda2798}$	2.25–2.31	1	3
NB_H	H $\alpha_{\lambda6563}$	1.44–1.48	6	21
	[O III]$_{\lambda\lambda4959,\,5007}$	2.19–2.29	3	16
NB_K	H $\alpha_{\lambda6563}$	2.21–2.25	8	20

LAEs at $z = 2.2$. Other line-emitters are classed using the criteria described in Table 3. We spectroscopically identify four interlopers ($\approx$15 $\pm$ 7 per cent contamination, similar to the 10 $\pm$ 4 per cent from Sobral et al. 2017). These comprise two C IV emitters at $z = 1.53$ and two AGN for which we measure Lyman-Werner and Lyman-Continuum radiation in the NB392 filter at $z = 3.16$ and $z = 3.57$. We also identify two dual-emitters that are missed by the colour–colour selection (see Fig. B1). This results in a final sample of 25 LAEs at $z = 2.2$.

4.2 Line-emitters in stV

The stV medium-band filter is used to identify LAEs at $z \approx 2.4$. Because the width of the filter is relatively broad, it is sensitive to line-emitters over a larger redshift space (and thus covers a larger volume), at the cost of being only sensitive to lines with high EW. We apply a selection criterion of $\rm EW_{obs} > 130$ Å (which corresponds to B_w −stV>0.54). We note that due to the width of the filter, it is possible that multiple lines contribute to the observed EW and line-flux, such as the combination of Ly α + N V.[5] It is therefore not straightforward to interpret measured EWs and line-fluxes and caution must be taken.

We find a total of 39 line-emitters, of which 15 have spectroscopic redshifts (see e.g. Table 2). As expected, these are not only dominated by LAEs at $z = 2.3$–2.45 but also contain high-ionization lines as C III] and C IV at $z \approx 1.1$–1.7. After removal of one spectroscopic contaminant (a C IV emitter at $z = 1.613$) selected with the colour criteria described in Table 3 and illustrated in Fig. B1, we obtain a sample of 16 LAEs.

[5] For example, for Type I AGN, N V/Ly α is typically $\approx$3 per cent (e.g. Vanden Berk et al. 2001), while for Type II AGN (such as narrow-line Seyferts) N V/Ly α can be as high as 50 per cent (typically $\approx$20 per cent, e.g. Alexandroff et al. 2013).

4.3 Line-emitters in NB501

The NB501 filter is used to select Ly α emitters at $z = 3.1$. We apply $\rm EW_{obs} > 50$ Å (g −NB501 >0.45), corresponding to a Lyα rest-frame EW of >12 Å.

We find a total of 65 line-emitters; of which only four have an archival spectroscopic redshift. This is because the majority of these line-emitters are faint with line-fluxes below 2×10^{-16} erg s^{-1} cm^{-2}. One spectroscopic confirmed line-emitter is a LAE, two are C IV emitters at $z = 2.24$ and $z = 2.26$ (these are the dual-emitters B-HiZELS_3 and B-HiZELS_15, Table C1, also detected as line-emitters in several other bands) and one is possibly [Ne V] at $z = 0.426$.

LAEs are selected as relatively blue U drop-outs (e.g. Hildebrandt et al. 2009) as described in Table 3 and illustrated in Fig. B2). One C IV emitter at $z = 2.24$ is misclassed as a LAE and is removed from the sample. This leads to a sample of 31 LAEs. We note that our EW criterion of $\rm EW_0 > 12$ Å is somewhat lower than the typical criterion used for selections of LAEs ($\rm EW_0 > 25$ Å; e.g. Ouchi et al. 2008; Yamada et al. 2012). However, more than 90 per cent of the identified LAEs have $\rm EW_0 > 25$ Å. Contrary to the properties of LAEs at $z \sim 2$, the additional LAEs with low EW are all faint in their UV continuum. This indicates an evolution in the properties of luminous LAEs from $z = 2$–3, with an increasing Ly α $\rm EW_0$ with redshift at fixed Ly α luminosity. Very recently, four additional LAEs from this sample have been confirmed at $z = 3.1$ from our spectroscopic follow-up campaign (to be presented in Sobral et al., in preparation), including the brightest LAE in our sample with a Lyα luminosity of $\approx 10^{43.8}$ erg s^{-1} ($\sim 10 \times L^\star$ at $z = 3.1$, Ouchi et al. 2008) in a 3 arcsec aperture and an $\rm EW_0$ of ∼150 Å. To the current surface brightness limit, it is extended over ∼5 arcsec (40 kpc), and it may thus be classed a Ly α blob (e.g. Matsuda et al. 2004; Prescott et al. 2008; Dey et al. 2016). This follow-up spectroscopy also identifies two interlopers: a red [O II] emitter at $z = 0.35$ and a Mg II emitter at $z = 0.81$, which we have removed from the sample.

4.4 Line-emitters in NB921

While the NB921 filter has been used to select LAEs at $z = 6.6$ (e.g. Matthee et al. 2015), it is also used to select H α, H β/[O III] and [O II] emitters at lower redshift (e.g. Ly et al. 2007; Drake et al. 2013; Sobral et al. 2013; Khostovan et al. 2015). We select 1161 line-emitters with the excess criterion of EW > 30 Å (corresponding to z −NB921>0.3).

Since our sample of line-emitters is selected from relatively deep narrow-band imaging (compared to the other narrow-bands in this survey), it is dominated by sources with fluxes fainter than 2×10^{-16} erg s^{-1} cm^{-2} (>94 per cent of line-emitters), down to fluxes of 2×10^{-17} erg s^{-1} cm^{-2}. Because of this, the number of spectroscopic redshifts is limited to only seven, of which five are H α emitters at $z = 0.4$. However, the number of galaxies with a robust redshift due to emission lines in multiple narrow-bands is significantly higher (23) (see Table 2).

Amongst our sample of line-emitters, we use colour criteria (Fig. B3; based on Sobral et al. 2013) to identify H α emitters at $z = 0.40$, H β/[O III] emitters at $z = 0.83$ and [O II] emitters at $z = 1.47$ (see Table 3). We select 198 H α emitters, 304 H β/[O III] emitters and 277 [O II] emitters (see Table 4). Two MgII emitters at $z = 2.26$ are misidentified as [O II] emitter, while one dual-emitter at $z = 1.47$ is misidentified as Hβ/[O III] emitters.

Table 3. Colour selection criteria used to classify line-emitters. These criteria are based on the expected positions of the Lyman and Balmer breaks [see for example the BzK criterion from Daddi et al. (2004)]. These criteria are then fine tuned using spectroscopic and dual-NB redshifts. In comparison to traditional criteria that use the B band, we adjust the B_w magnitude for the contribution from flux in the U band. For samples at $z > 2.4$, we also include a colour criterion that removes very red objects for which the Lyman-break criterion has selected a strong Balmer break [see also Xue et al. (2017)]. The colour–colour selections are illustrated in the figures in Appendix B.

Filter	Emission line	Colour criterion
NB392	Ly α $z = 2.2$	$(2B_w - U) - z < 0.2 + 0.7(z - K)$
stV	Ly α $z = 2.4$	$U - B_w > 0.3(B_w - g) + 0.2$ & $g - I < 1$
NB501	Ly α $z = 3.1$	$U - g > 1$ & $g - I < 1.5$
NB921	H α $z = 0.40$	$(2B_w - U) - I > 0.4 + 0.4(Z - H)$ & $B_w - R > 1.3(R - I)$
	[O III]/H β $z = 0.80$	$(2B_w - U) - I > 0.4 + 0.4(Z - H)$ & $B_w - R < 1.3(R - I)$
	[O II] $z = 1.47$	$(2B_w - U) - I < 0.4 + 0.4(Z - H)$
NB_H	$z > 1$	$(2B_w - U) - z < 0.4 + 0.8(z - K)$ or $z - K > 2$
	H α $z = 1.47$	$z > 1$ & $J - K < 2.1(I - J) - 1$
	[O III]/H β $z = 2.23$	$z > 1$ & $J - K > 2.1(I - J) - 1$
	[O II] $z = 3.3$	Not H α or [O III]/H β in NB_H & $U - g > 1$ & $g - I < 1.5$
NB_K	$z > 1$	$(2B_w - U) - z < (z - K) - 0.05$ or $z - K > 2$
	H α $z = 2.23$	$z > 1$ & $U - R < 2$
	[O III]/H β $z = 3.2$	$z > 1$ & $U - g > 1$ & $g - I < 1.5$
	[O II] $z = 4.7$	Not H α or [O III]/H β in NB_K & $g - I > 1.5$

Table 4. Line identifications of the total ∼2000 emitters (as described in Section 4) in the Boötes-HiZELS narrow-band filters.

Filter	Subsample	# of sources
NB392	$\Sigma > 3$, EW > 30 Å	57
	Ly α at $z = 2.23$	25
stV	$\Sigma > 3$, EW > 130 Å	39
	Ly α at $z = 2.4$	16
NB501	$\Sigma > 3$, EW > 50 Å	65
	Ly α at $z = 3.1$	32
NB921	$\Sigma > 3$, EW >30 Å	1161
	H α at $z = 0.40$	198
	[O III]/H β at $z = 0.8$	304
	[O II] at $z = 1.47$	277
NB_H	$\Sigma > 3$, EW >85 Å	301
	H α at $z = 1.47$	87
	[O III]/H β at $z = 2.23$	72
	[O II] at $z = 3.3$	6
NB_K	$\Sigma > 3$, EW >80 Å	255
	H α at $z = 2.23$	77
	[O III]/H β at $z = 3.2$	11
	[O II] at $z = 4.7$	2

Due to their faintness, 359 out of the 1161 line-emitters are not detected in a sufficient number of broad-bands required for classification and can thus not be classed. We expect that most of these sources are faint H α, H β/[O III] or [O II] emitters. Based on the fraction of emitters in different classifications as a function of line-flux, we expect an increasing fraction of [O II] emitters at low line-fluxes (see also Sobral et al. 2012). As illustrated in the left-hand panel of Fig. 2, the majority of sources indeed has $B_w - R$ colours similar to [O II] emitters (but could not be classed due to their faintness in other broad-band filters). We discuss this 'identification incompleteness' further in Section 5.1.3.

4.5 Line-emitters in NB_H

We select line-emitters detected in the NB_H filter with a narrow-band excess of EW >85 Å (corresponding to H $-NB_H > 0.3$). Since the near-infrared detectors of UKIRT/WFCAM contain significant amounts of cross-talk, we perform careful visual inspections of our sample of line-emitters, resulting in a sample of 301 line-emitters.

While the sample of line-emitters includes nine sources with spectroscopic redshifts (six H α at $z = 1.4$ and three H β/[O III] at $z = 2.2$), the NB_H line-emitters are particularly suitable for identifying line-emitters with the dual-NB technique. These robustly identified line-emitters are used to adapt the colour selection criteria from Sobral et al. (2013) for the data available in this field. Using the criteria listed in Table 3, we select 87 H α emitters at $z = 1.47$, 72 H β/[O III] emitters at $z = 2.2$ and 6 [O II] emitters at $z = 3.3$ (see Table 4). 99 sources are classed as low-redshift interlopers and 39 sources are too faint to be detected in the required broad-bands. Prior to the final identification, four spectroscopically confirmed H β/[O III] emitters were classed as H α emitters, while five H α emitters were classed as H β/[O III] emitter. These misidentified emitters are typically very luminous and likely AGN, such that their colours are anomalous (see Fig. B4). There are no such identified contaminants amongst the fainter dual-emitters.

4.6 Line-emitters in NB_K

We select line-emitters detected in the NB_K filter with EW >80 Å (corresponding to $K - NB_K > 0.23$). In total, after visual inspections, we find 255 line-emitters, of which 18 have a spectroscopic redshift (including eight H α at $z = 2.23$) and 20 are dual-emitters (all H α at $z = 2.23$). Based on these robust redshifts and the colour selection criteria listed in Table 3, we select 77 H α emitters at $z = 2.2$, 11 H β/[O III] emitters at $z = 3.2$ and 2 [O II] emitters at $z = 4.7$ (see Table 4). 110 line-emitters are at $z < 1.5$ and 55 line-emitters are too faint to be classified. We have not identified any spectroscopically confirmed contaminants before the final classification. However, the colour–colour criteria missed two X-ray-detected dual-emitters at $z = 2.23$, as illustrated in Fig. B5.

5 NUMBER DENSITIES

5.1 Method

We measure the number densities of LAEs at $z = 2.2$, 2.4 and 3.1, H α emitters at $z = 0.4$, 1.47 and 2.23, Hβ/[O III] emitters at $z = 0.8$,

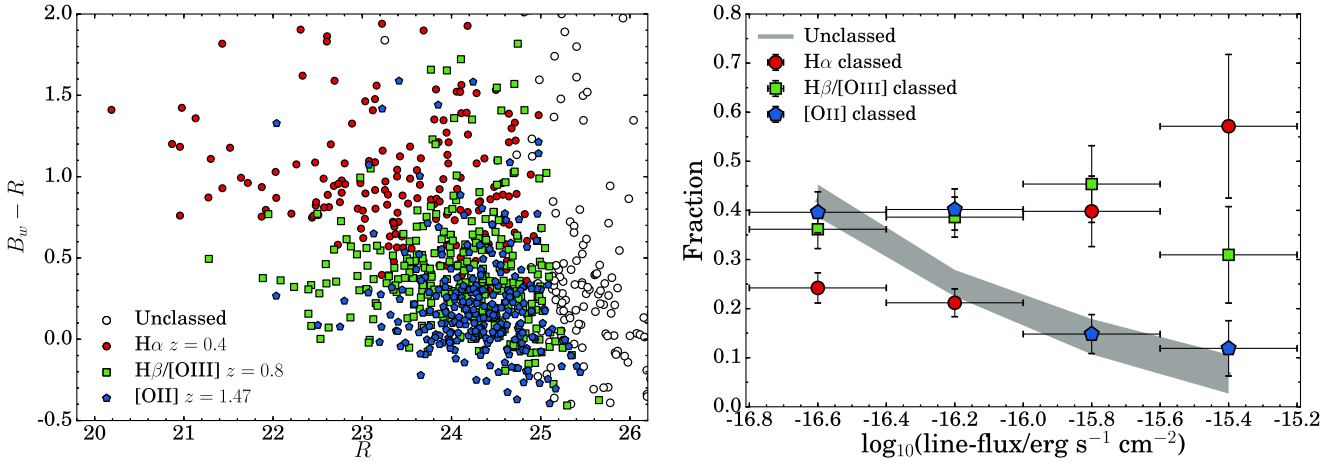

Figure 2. Left: $B_w - R$ versus R colour–magnitude diagram of line-emitters in NB921. This plot illustrates that the line-emitters that are not detected in enough broad-bands (such as I, z or H) in order to be classified, are typically faint ($R > 25.5$, note that these are low S/N detections) and lie most closely to the colour–magnitude parameter space probed filled with [O II] emitters. Right: the fraction of sources classed as Hα, Hβ/[O III] and [O II] amongst the classed NB921 line-emitters in bins of line-flux. The grey-shaded area shows the fraction of sources that is unclassed and its Poissonian uncertainty. All emitters at higher line-fluxes are classed. These fractions are used to correct for identification incompleteness (Section 5.1.3).

Table 5. Survey volumes and flux completenesses for the various line-emitters in this survey.

Filter	Emission line	Volume (10^5 Mpc^3)	50 per cent completeness (erg s^{-1} cm^{-2})
NB392	Lyα $z = 2.2$	2.8	1.3×10^{-16}
stV	Lyα $z = 2.4$	9.5	4.7×10^{-16}
NB501	Lyα $z = 3.1$	7.2	1.1×10^{-16}
NB921	Hα $z = 0.4$	0.2	1.0×10^{-16}
	Hβ/[O III] $z = 0.8$	1.2	1.0×10^{-16}
	[O II] $z = 1.47$	1.7	1.0×10^{-16}
NB_H	Hα $z = 1.47$	2.5	1.3×10^{-16}
	Hβ/[O III] $z = 2.2$	5.2	1.3×10^{-16}
NB_K	Hα $z = 2.2$	2.7	0.5×10^{-16}

2.2, 3.2 and [O II] emitters at $z = 1.47$, 3.3, 4.7 as a function of their line luminosity, in narrow luminosity bins (0.2–0.3 dex in this analysis). The luminosity is calculated using the line-flux (Section 3.3) and assuming the luminosity distance corresponding to the redshift of peak filter transmission for the relevant emission line. We calculate the comoving volume for each line/filter combination using the redshifts of half peak transmission (see Table 5). For Hβ/[O III], we compute the volume following Khostovan et al. (2015), who uses only the volume probed by the [O III]$_{\lambda 5007}$ line. We refer to this work and Sobral et al. (2015) for a detailed discussion on the contribution of Hβ and [O III]$_{\lambda 4959}$. Luminosity-binned number densities were calculated by dividing the number of sources in each bin by the comoving volume, and then correcting these (as described in the following subsections) for the effects of the filter profile, flux incompleteness and identification incompleteness. Uncertainties on these number densities were estimated using Poissonian errors. To be conservative, we add in quadrature 20 per cent of the flux completeness correction and 20 per cent of the identification-incompleteness correction (in the case of the red narrow-bands) to the error of each bin. We only show bins with >40 per cent flux completeness.

5.1.1 *Filter profile correction*

As described in Khostovan et al. (2015) and Sobral et al. (2013, 2015), observed number densities have to be corrected for the fact that the filter transmission curves are not a perfect top-hat. Because of this, luminous sources may be observed as faint sources if they lie at a redshift corresponding to the wings of the filter. Furthermore, at fixed flux-limit, fainter sources can only be observed over a smaller volume than more luminous sources. Following the method described in these papers, we compute the number density corrections using a simulation. This simulation assumes that sources are distributed randomly in redshift space and computes their observed luminosities based on the relevant filter transmission. We then obtain a volume correction for each luminosity bin. These corrections typically increase the number densities of the most luminous bins by at most 0.3 dex, while the number densities of fainter bins stay constant, or are decreased by at most 0.05 dex.

5.1.2 *Detection flux completeness*

The flux completeness of our selection is measured as a function of line-flux as follows: for the relevant line, we select galaxies that are not selected as a line-emitter, but do fulfil the colour criteria from Section 4. We then artificially add line-flux (starting from 10^{-18} erg s^{-1} cm^{-2} in steps of 0.05 dex) and recompute the line excess and excess significance for each step. After each step, we measure the fraction of sources that would be selected as line-emitter with the added line-flux. We tabulate the 50 per cent completeness in Table 5. Most narrow-band selections are 50 per cent complete at $\sim 1 \times 10^{-16}$ erg s^{-1} cm^{-2}, with the exception of stV, which is only sensitive to brighter emission lines.

5.1.3 *Identification incompleteness*

For the red narrow-bands, we also take into account that the broad-band data are not deep enough for a robust classification of all faintest line-emitters, which we call identification incompleteness. We estimate corrections for this effect as follows: for each narrow-band filter, we measure the fraction of line-emitters that is classed

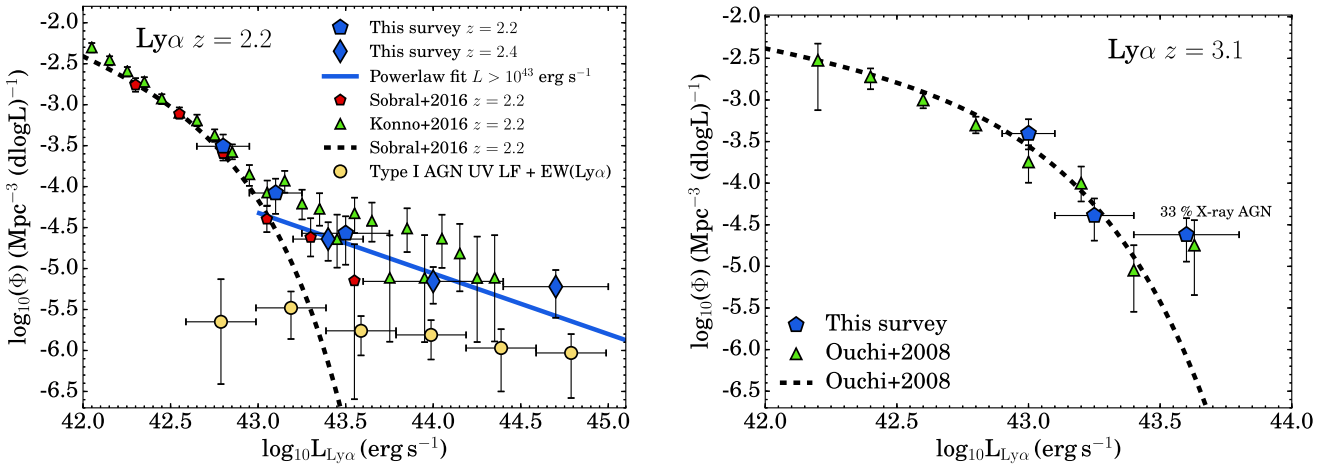

Figure 3. Number densities and LFs of LAEs at $z \approx 2.2$ and $z = 3.1$. The power law like behaviour at the bright end is due to the contribution from AGN (for which we provide a fit in Section 5.2.1). The yellow points show an estimate of the contribution from Type I AGN, based on the UV LF combined with a Ly α of 80 Å. At $z \approx 2.2$, we find good agreement between the LF of LAEs in B-HiZELS and the LF we measured in Sobral et al. (2017) and to the survey from Konno et al. (2016). The number density of LAEs at $z = 3.1$ is similar to that measured by Ouchi et al. (2008) in the UDS field.

as either H α, H β/[O III] or [O II] emitter or as lower redshift source, as a function of line-flux and assume that this fraction can be extrapolated to the line-fluxes of the sources that are not classable.

We find that for line-emitters in NB921 the fraction of classed H α, H β/[O III] and [O II] emitters is 25 ± 5, 35 ± 5 and 40 ± 4 per cent, respectively, at fluxes $<6.3 \times 10^{-17}$ erg s^{-1} cm^{-2} and 42 ± 10, 38 ± 10 and 20 ± 8 per cent, respectively, for fluxes between 6.3×10^{-17} and 4×10^{-16} erg s^{-1} cm^{-2} (see Fig. 2). This is expected, as sources with fainter fluxes are expected to be at higher redshift. For line-emitters in NB_H, the corresponding fractions are 25 ± 5, 25 ± 7 and 4 ± 2 per cent at fluxes below 4×10^{-16} erg s^{-1} cm^{-2}. This means that ∼40 per cent of the unclassed sources is likely at $z < 1$. Above this flux, all sources are classed. These fractions are in agreement with the estimate from Sobral et al. (2012). Finally, for line-emitters in NB_K, we estimate that below a flux of 1.5×10^{-16} erg s^{-1} cm^{-2} a fraction of 40 ± 8 per cent of the line-emitters is H α, 7 ± 3 per cent is H β/[O III], while 55 ± 6 per cent is at low redshift. All sources with a larger line-flux have been classed. We note that maximally 40 per cent of the sources in a flux bin are unclassed. This maximum occurs in the faintest bin of the NB921 line-emitters (see Fig. 2). The typical fraction of unclassed sources at the discussed flux levels is 20 per cent. We use the estimates described above to obtain the identification incompleteness for each luminosity bin for the relevant emission line.

5.2 Comparison with previous surveys

5.2.1 Lyman-α emitters at z = 2.2–3.1

We show the measured LF of LAEs at $z = 2.2$–2.4 and $z = 3.1$ in Fig. 3. The depth of our data allows us to constrain the LF to $\approx L^\star$. We find good agreement with earlier results from Sobral et al. (2017) and those from Konno et al. (2016) in different survey fields and slightly different colour criteria (see also An et al. 2016). All surveys indicate that the Ly α LF at $z \approx 2.2$ deviates from a Schechter function at bright luminosities.[6] We note that all LAEs at $z = 2.2$ with a luminosity above 10^{44} erg s^{-1} are either spectroscopically confirmed or have a dual-NB redshift. As discussed in Sobral et al. (2017), the power-law behaviour of the LF is likely due to the contribution of AGN in addition to the normal Schechter function. Indeed, most (∼80 ± 40 per cent) luminous LAEs ($L_{Ly\alpha} > 10^{43}$ erg s^{-1}) are AGN (either due to X-ray detection or C IV detection in NB501). We fully explore this in Section 6.4.

Due to its larger probed cosmic volume, the stV filter is mostly sensitive to very luminous LAEs. Although all LAEs with a luminosity above 10^{44} erg s^{-1} at $z = 2.4$ are spectroscopically confirmed, we expect that the sample with luminosities 10^{43-44} erg s^{-1} is contaminated, as the spectroscopic follow-up at these fluxes is not complete. Most importantly, we expect contaminants to be emission lines that are associated with AGN activity such as C IV, C III] and He II at $z = 1.15$–1.65 (e.g. Stroe et al. 2017), which are challenging to identify with these colour–colour selections. We estimate the contamination at these flux levels by mimicking the selection of this survey in a similar medium band in the COSMOS field (IA427, Santos et al., in preparation). We select LAEs at $z = 2.5$ with the same criteria (including broad-band depths) and estimate the number of interlopers using the most recent photometric redshifts (Laigle et al. 2016) and a compilation of spectroscopic redshifts. We find that at luminosities $\sim 10^{43-44}$ erg s^{-1}, there is a non-negligible contamination due to C IV, C III] and HeII emitters of 20±10 per cent. At higher luminosities, the contamination decreases to 4 ± 4 per cent. The plotted number densities are corrected for these contamination rates. We combine the $z = 2.2$–2.4 data to fit a power-law function to the number density of LAEs at the bright end ($L_{Ly\alpha} > 10^{43}$ erg s^{-1}), which results in $\log_{10}(\Phi) = 27.5^{+7.3}_{-7.4} - 0.74^{+0.17}_{-0.17} \log_{10}(L_{Ly\alpha})$, with a reduced χ^2 of 1.1. This fit is slightly shallower than the power law fitted by Sobral et al. (2017) based on a smaller volume, but consistent within 1σ.

We estimate the contribution of broad-line Type I AGN to the Ly α LF at $z \approx 2.2$ based on the UV LF of Type I AGN at $2.0 < z < 2.5$ from Bongiorno et al. (2007) and the typical UV slope and Ly α EW of these AGN. Assuming $f_\lambda \propto \lambda^{-1.5}$ and Ly α $EW_0 = 80$ Å (e.g. Vanden Berk et al. 2001; Hunt et al. 2004), we convert the number densities as a function of M_{1450} to number densities as a function of Ly α luminosity. As shown in Fig. 3, it is clear that the number density of LAEs is higher than the number density of Type I

[6] The Schechter (1976) shape of the LF is expressed as $\Phi(L)\, dL = \Phi^\star (\frac{L}{L^\star})^\alpha e^{-\frac{L}{L^\star}} d(\frac{L}{L^\star})$, where $\Phi^\star$ is the characteristic number density, $L^\star$ is the characteristic luminosity and α is the faint-end slope.

AGN at fixed Ly α luminosity. This indicates that only a fraction of the luminous LAEs are likely Type I AGN. This estimate suggests that at Ly α luminosities 10^{43-44} erg s^{-1} the fraction of Type I AGN is only $\sim$10 per cent, while the fraction is $\sim$20–30 per cent at higher Ly α luminosities. Because the AGN LF at the faintest UV magnitudes is relatively flat, these fractions do not depend strongly on the assumed values of the Ly α EW or UV slope. The low Type I AGN fraction indicates that the majority of luminous LAEs are narrow-line Type II AGN (see also Section 6.4), or star-forming galaxies.

At $z = 3.1$, we find that the Ly α LF agrees well with that from Ouchi et al. (2008), who performed a deep Ly α survey over a similar area. Compared to similar NB501 data in the COSMOS field (with deeper ancillary data and relatively more spectroscopic follow-up; Matthee et al., in preparation), we also find that the fraction of line-emitters (with similar line-flux and EW distributions) that are classed as LAE is similar: 51 $\pm$ 9 per cent in Boötes against 46 $\pm$ 7 per cent in COSMOS. This also confirms evolution in $L^\star$ between $z = 2.2$–3.1 from $L_{\mathrm{Ly}\,\alpha} \approx 4 \times 10^{42}$ erg s^{-1} to $L_{\mathrm{Ly}\,\alpha} \approx 9 \times 10^{42}$ erg s^{-1}. The number density of LAEs in the brightest bin (three out of the four sources in this bin are spectroscopically followed-up and confirmed) lies above the Schechter fit from Ouchi et al. (2008) (similar to the actual data points from that survey), indicating the presence of AGN amongst these luminous sources, similar to $z \sim 2$. Indeed, we find evidence for AGN activity for most LAEs in the most luminous bin, either due to an X-ray detection or due to the detection of high ionization emission lines as [Ne IV]$_{\lambda 2424}$ or broad Si IV and C IV absorption features in the spectrum (Sobral et al. in preparation).

5.2.2 *H α emitters at* z = *0.4–2.2*

We show the number densities of H α emitters as a function of their observed H α luminosities. The H α luminosities are corrected for the contribution due to [N II] following a method based on observed H α+[N II] EW (Sobral et al. 2012). H α luminosities are not corrected for attenuation due to dust and we compare our results with dust-uncorrected values from the literature. In case dust-uncorrected values are not provided, we convert dust-corrected values back using the prescriptions outlined in the relevant papers.

As illustrated in Fig. 4, we find that the H α LF at $z = 0.4$, 1.47 and $z = 2.23$ are generally in good agreement with the number densities in the UDS+COSMOS parts of the HiZELS survey from Sobral et al. (2013). Within the errors, the LF agrees well with the fitted relations from Drake et al. (2013) and Ly et al. (2007). At $z = 2.23$, the number densities complement the number densities at fainter luminosities from Lee et al. (2012). This confirms strong evolution in $L^\star_{\mathrm{H}\,\alpha}$ from $z = 0.4$–2.23. We note that at $z = 0.4$ there could be some contamination at the faintest luminosities due to identification incompleteness (see Section 5.1.3). At $z = 1.47$, the luminosities seem to be systematically higher by $\approx$0.1–0.15 dex, increasing slightly with luminosity. This offset can partly be explained by different apertures used in the photometry. While Sobral et al. (2013) uses 2 arcsec apertures for all measurements above $z > 0.5$, we use 3 arcsec measurements. Redoing the measurements with 2 arcsec apertures (smaller symbols in Fig. 4) results in good agreement at our faintest luminosities and reasonable agreement (within the error bars) at higher luminosities. At faint luminosities, the luminosity difference between the two apertures is typically 0.14 dex, while it is typically 0.1 dex at high luminosities. The highest luminosity bins at $z = 1.47$–2.23 show number densities diverging from a Schechter function, contributing to the difference as well. The sources in these bins are all spectroscopically confirmed or have dual-NB redshifts and most are X-ray detected, as indicated in the corresponding panels. We discuss this in more detail in Section 6.4.

Compared to the grism results at $0.3 < z < 0.9$ from Colbert et al. (2013), the number densities at $z = 0.4$ are offset (mostly in terms of luminosity). This can simply be explained by the evolution in the typical H α luminosity between $z = 0.4$ and the median redshift of the Colbert et al. (2013) sample of $z \approx 0.6$, as $\log L^\star_{\mathrm{H}\,\alpha}$ increases with $0.45 \times z$ over this redshift range (Sobral et al. 2013). The number densities at $z = 1.47$ are in good agreement with the grism results at $0.9 < z < 1.5$, even though the median grism redshift is $z \approx 1.2$. This indicates that there is little evolution in $L^\star_{\mathrm{H}\,\alpha}$ between $z = 1.47$ and $z \approx 1.2$.

5.2.3 *H β/[O III] emitters at* z = *0.8–3.2*

We also compare our identification of H β/[O III] at $z = 0.8$, 2.2, 3.2 with the analysis from Khostovan et al. (2015) in the COSMOS and UDS fields.

As illustrated in Fig. 4, the number densities of H β/[O III] emitters at $z = 0.8$ are in good agreement with those from Khostovan et al. (2015), and higher than those from Ly et al. (2007) and Drake et al. (2013), which could be due to cosmic variance or systematics such as different apertures and estimates of volume and completeness. Using a large 10 deg^2 H α, H β/[O III] and [O II] survey, Sobral et al. (2015) estimated empirically that the uncertainty in $L^\star$ and $\Phi^\star$ due to cosmic variance over the volume probed in these surveys at $z = 0.8$ is $\approx$40–50 per cent. Such variance could easily explain the observed differences. At $z = 2.2$, the number densities are systematically higher in luminosity compared to the literature results. Similarly as in Section 5.2.2, we find that this is partly due to an aperture effect. As expected, the difference in luminosities measured with different apertures is slightly smaller at $z = 2.2$ than at $z = 1.47$, with a typical luminosity difference of 0.11 dex. As a consequence, even when matching apertures to Khostovan et al. (2015), we still find an offset at fainter luminosities, which we attribute to cosmic variance. Although the number of H β/[O III] emitters at $z = 3.2$ is limited, their number densities agree well with those from Khostovan et al. (2015).

Unlike the H α number densities, the number densities of Hβ/[O III] emitters are in good agreement with those from Colbert et al. (2013), which could indicate that there is less evolution in the Hβ/[O III] LF than in the H α LF between $0.7 < z < 1.5$. However, this could also be due to the contribution of H β emitters (see Sobral et al. 2015 and Khostovan et al. 2015 for detailed discussions). Except for luminosities $>10^{43}$ erg s^{-1}, the number densities of H β/[O III] emitters at $z = 0.8$ are a factor 30–100 higher (at fixed [O III] luminosity) than the number densities of Type II AGN at $z \sim 0.71$ (Bongiorno et al. 2010).

5.2.4 *[O II] emitters at* z = *1.47, 3.3, 4.7*

Fig. 5 compares the number density of [O II] emitters at $z = 1.47$, 3.3, 4.7 to the other published results. At $z = 1.47$, the number densities agree reasonably well with Drake et al. (2013) and Khostovan et al. (2015), except for the faintest bin, although identification incompleteness is significant in this bin. At the bright end, the Schechter fit from Ly et al. (2007) indicates a lower number density, potentially due to a lack of bright sources in a small survey volume.

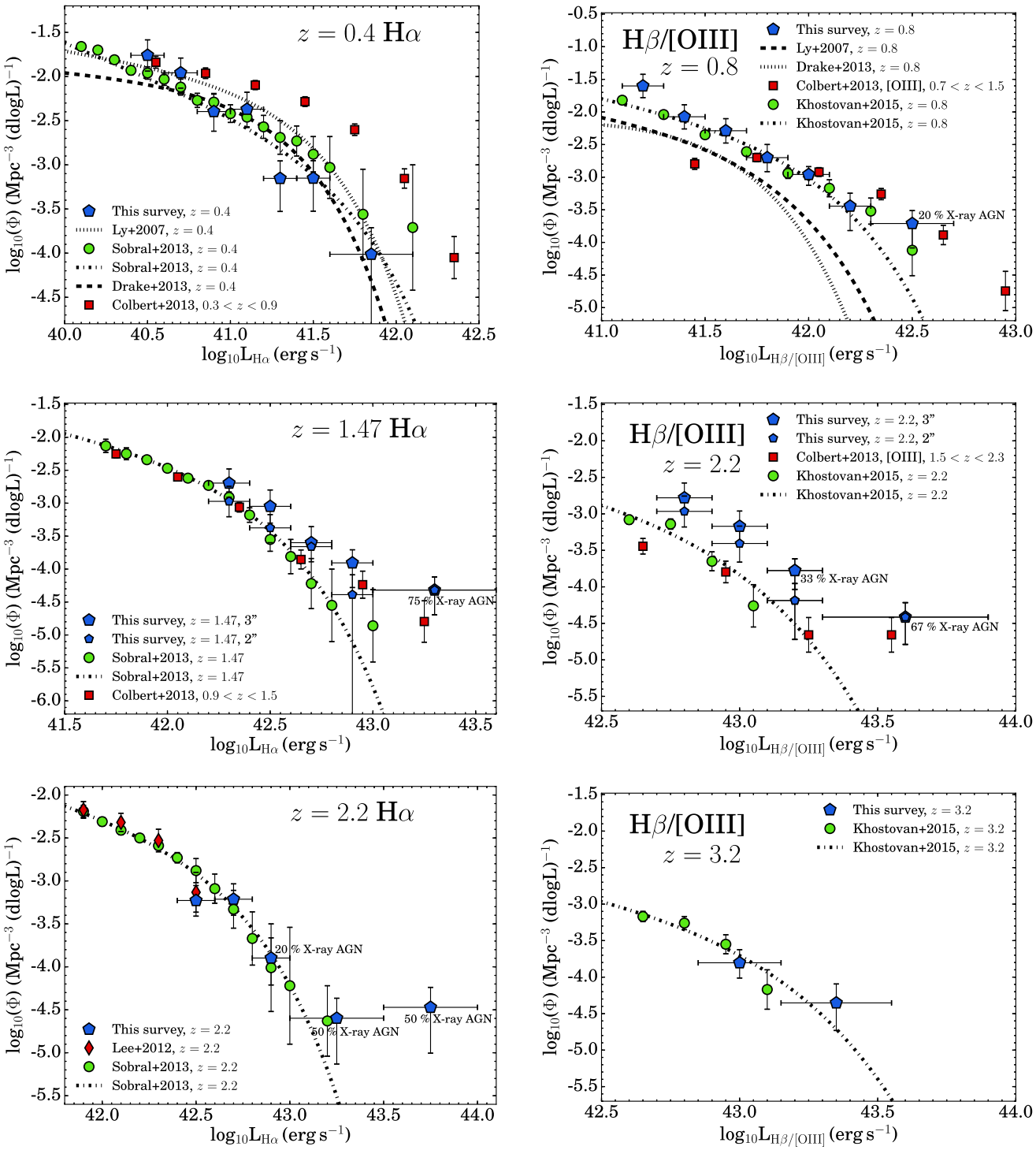

Figure 4. Left column: measured H α LFs at $z = 0.4$, 1.47, 2.2. H α luminosities are corrected for the [N II] contribution using a relation with Hα+[N II] EW (Sobral et al. 2012), but are not corrected for dust. At $z = 0.4$, the LF is compared to the narrow-band survey from Ly et al. (2007) in the Subaru Deep Field (SDF) field and Drake et al. (2013) in the UDS field and with the survey from Lee et al. (2012) at $z = 2.2$. At all redshifts, the number densities are compared to the HiZELS survey results in the UDS+COSMOS fields from Sobral et al. (2013). We also compare the LFs with those measured in a blind grism survey by Colbert et al. (2013). Overall, there is reasonable agreement. The luminosity-offset at $z = 1.47$ may be explained by aperture effects (see Section 5.2.2). The brightest bin at $z = 2.2$ is due to the presence of (spectroscopically confirmed) AGN. Right column: measured Hβ/[O III] LFs at $z = 0.8$, 2.2, 3.2, compared to Ly et al. (2007) and Drake et al. (2013) at $z = 0.8$ and to Khostovan et al. (2015) and Colbert et al. (2013) at higher redshift. There is a luminosity-offset at $z = 2.2$ that is partially due to a larger aperture measuring a higher luminosity by ≈0.14 dex (this is the same filter as the Hα LF at $z = 1.47$). The brightest bin at $z = 2.2$ contains the same AGN as in the brightest bin of the H α LF at $z = 2.2$.

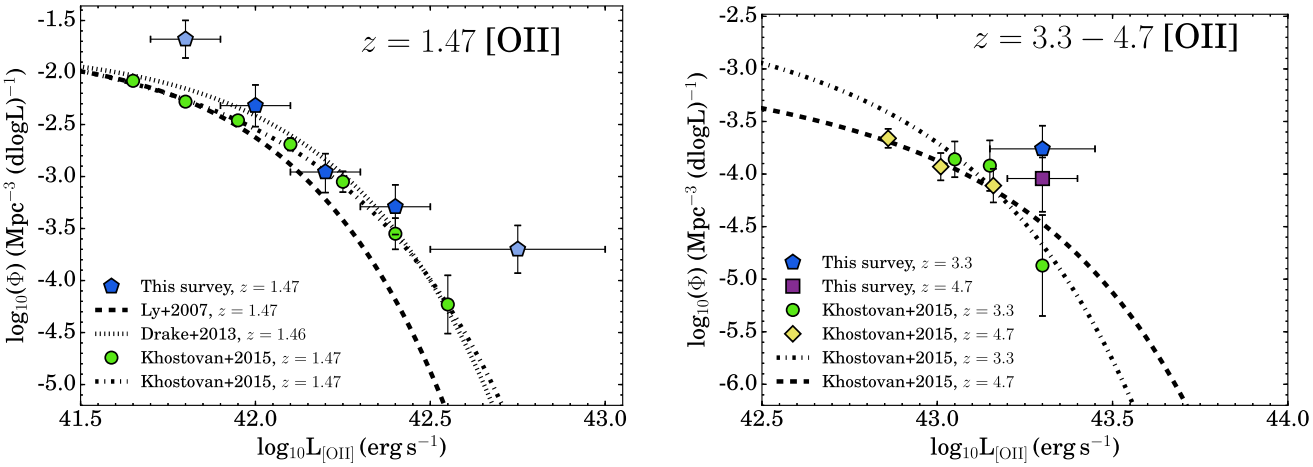

Figure 5. Measured [O II] LFs at $z = 1.47$, 3.3, 4.7. At $z = 1.47$, the LF shows reasonable agreement with those from Ly et al. (2007), Drake et al. (2013) and Khostovan et al. (2015), except at the bright end. Since the sources in the brightest bin are not spectroscopically confirmed and identification incompleteness in the faintest bin is large, we show these bins in a slightly lighter colour. We plot the number densities of [O II] emitters at $z = 3.3$ and $z = 4.7$ in a single panel. These number densities are slightly higher than Khostovan et al. (2015), potentially indicating some contamination or cosmic variance.

We note that the sources in the brightest bin are not spectroscopically confirmed and thus could be interlopers (for this reason, these points have a lighter colour in Fig. 5). Although the number of [O II] emitters in our samples at $z = 3.3$ and $z = 4.7$ is limited to a handful, their number densities are slightly higher than Khostovan et al. (2015), potentially indicating either contamination or cosmic variance. A further hint of contamination in this sample is that some have relatively low colour-excess (Fig. 6), which is unexpected for high-redshift sources, although this would also be consistent with a drop in typical EWs for [O II] emitters (Khostovan et al. 2016).

6 PROPERTIES OF LINE-EMITTERS

6.1 Dual-emitters

In total, we detect 42 line-emitters that are line-emitters in multiple narrow-bands. We list the coordinates, redshifts and -band magnitude of these line-emitters in Table C1. The majority (20) of dual-emitters are Hα+[O II] emitters at $z = 1.47$ detected in NB921 and NB$_H$, followed by 17 Hα+[O III] emitters at $z = 2.23$, of which two are also detected in Lyα, three in C IV and one in Mg II. Three galaxies are identified as LAE in NB392 at $z \sim 2.2$–2.3 and are also detected in either NB$_H$ ([O III]) or NB$_K$ (Hα), of which one is also detected in NB501 (C IV).

6.2 The most luminous Hα emitters at z = 2.23

B-HiZELS_1 is the most luminous Hα emitter known from HiZELS at $z = 2.23$ (i.e. Sobral et al. 2016) and also detected as Lyα and [O III] emitter. Although its high luminosity ($L_{H\alpha} = 7.9 \times 10^{43}$ erg s^{-1}) suggests that it is an AGN, it is X-ray undetected ($L_X < 3 \times 10^{44}$ erg s^{-1}, or $< L_X^\star$; La Franca et al. 2005). There is also a dual-emitter (B-HiZELS_27), detected in [O III] and Hα at the same redshift only 6 arcsec away (a projected distance of $\sim$50 kpc). This source has an estimated Hα EW$_0$ of $\gtrsim$400 Å and [O III] EW$_0 \gtrsim$ 375 Å. This places it at the very high end of the Hα EW distribution at $z = 2.2$ (Fumagalli et al. 2012; Sobral et al. 2014), and the galaxy is thus likely a low-mass extreme emission-line galaxy (e.g. van der Wel et al. 2011). These strong emission lines could indicate that this galaxy may be undergoing high interaction-induced SFR combined with little extinction due to dust, or is a shocked gas cloud.

The second most luminous Hα emitter at $z = 2.2$ is B-HiZELS_15 at $z = 2.244$ ($L_{H\alpha} = 3.6 \times 10^{43}$ erg s^{-1}). We also detect [O III], Hα and C IV emission lines (there are no Lyα observations at its position). Although B-HiZELS_15 also has a neighbouring galaxy (at $z = 2.242$ and a projected separation of $\approx$50 kpc) and the Hα luminosity is only a factor of 2 lower than that of B-HiZELS_1, several other properties are different. B-HiZELS_15 is X-ray detected, has a higher Hα EW$_0$ (360 Å versus 120 Å) and is more than three magnitudes fainter in the optical and NIR continuum. This indicates a diversity in the properties of luminous Hα emitters, similar to the results from Sobral et al. (2016).

6.3 [O II]–Hα view at z = 1.47

One strength of the Boötes-HiZELS survey is our sample of dual-emitters that can be used to study the relation between different star-formation rate indicators at $z = 1.47$ and $z = 2.23$, such as [O II], Hα and continuum tracers such as the rest-frame UV, FIR and radio. Compared to Hα, the [O II] emission line and UV continuum are more sensitive to dust attenuation and effects from metallicity and gas density (e.g. Kennicutt 1998; Jansen, Franx & Fabricant 2001; Ly et al. 2012), which may all evolve with redshift. We exploit this sample to derive the observed [O II]/Hα ratio at $z = 1.47$ and compare it to a reference sample from SDSS at $z = 0.1$, to test claims based on smaller samples by e.g. Hayashi et al. (2013) and Sobral et al. (2012).

We combine the sample of dual-emitters at $z = 1.47$ in Boötes with those from HiZELS in the UDS and COSMOS field (see Sobral et al. 2013 for details), and remove any source that is detected in the X-rays. In total, this results in a sample of 340 dual-emitters at $z = 1.47$. The majority of these are dominated by faint emitters observed in the deeper imaging in COSMOS. Hα luminosities are corrected for the contribution from the adjacent [N II] doublet using the relation with EW described in Sobral et al. (2012) (see also Sobral et al. 2015 for a spectroscopic validation). As a comparison sample at low redshift, we use a sample of emission-line

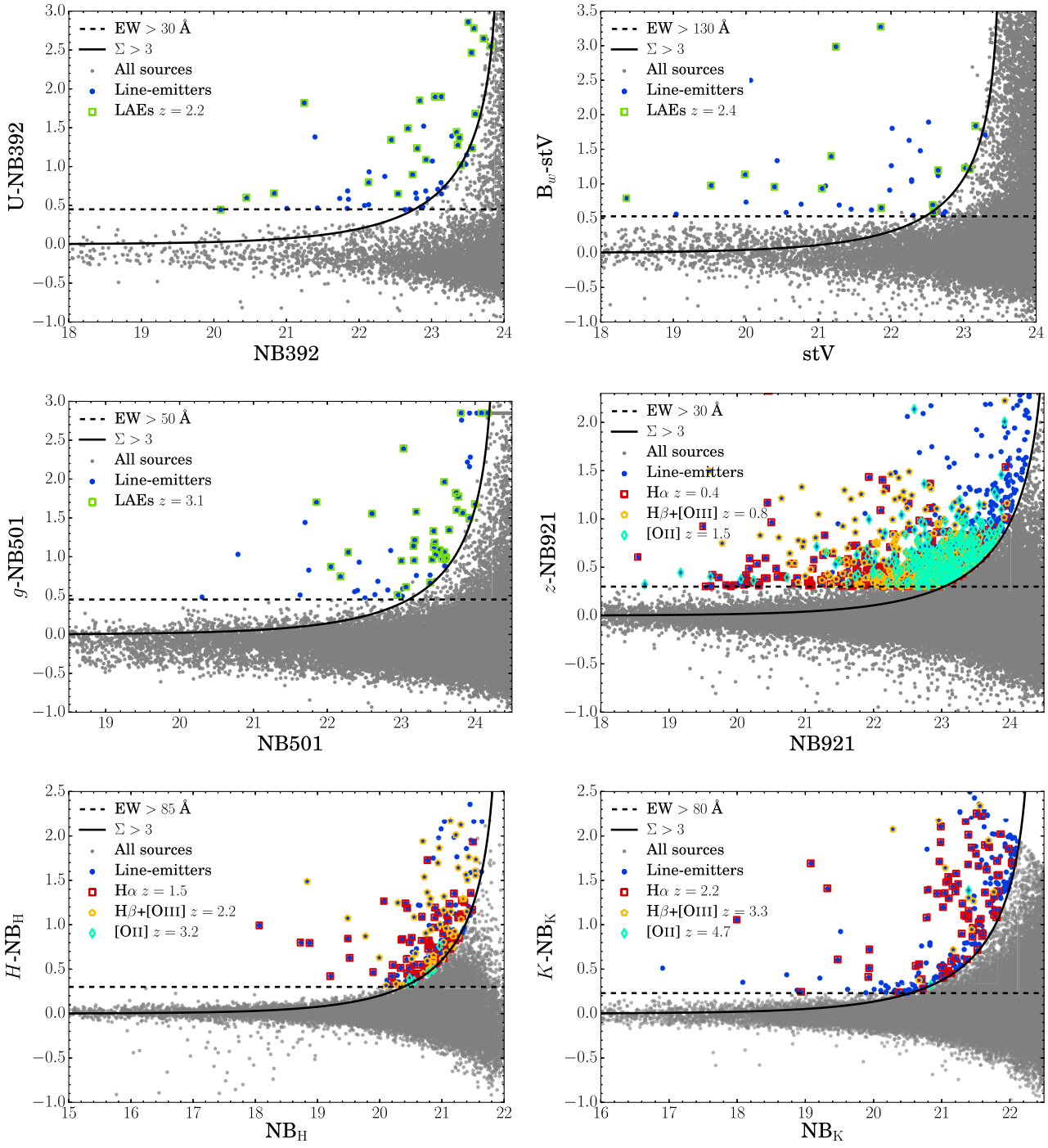

Figure 6. Narrow-band excess diagrams in NB392, stV, NB501, NB921, NB_H and NB_K. In grey, we show all detected sources, while blue points are sources selected as line-emitters. The horizontal dashed line shows the imposed EW selection cut, while the solid line shows the excess significance criteria for the typical depth of the survey. In the three blue filters, we mark Ly α selected sources with a green square. In the three red filters, we mark H α emitters with a red square, H β/[O III] emitters with a yellow pentagon and [O II] emitters with a blue diamond. We note that we compute the excess significance locally, such that some sources may lie above the selection line, but are not selected as line-emitters because they are in shallower regions. It can be seen that LAEs detected in NB392 and NB501 are typically identified if a line-emitter has a high excess and faint magnitude (because most are likely faint star-forming galaxies with high EW), while this is not the case for LAEs identified in stV (which are typically bright AGN). In NB921, it can clearly be seen that most unidentified line-emitters are amongst the faintest magnitudes and that there is a clear trend that higher redshift line-emitters are fainter and have higher observed EWs. In NB_H and NB_K H α emitters and H β/[O III] emitters have similar narrow-band magnitudes, but H β/[O III] emitters tend to have higher excess because they are at higher redshift.

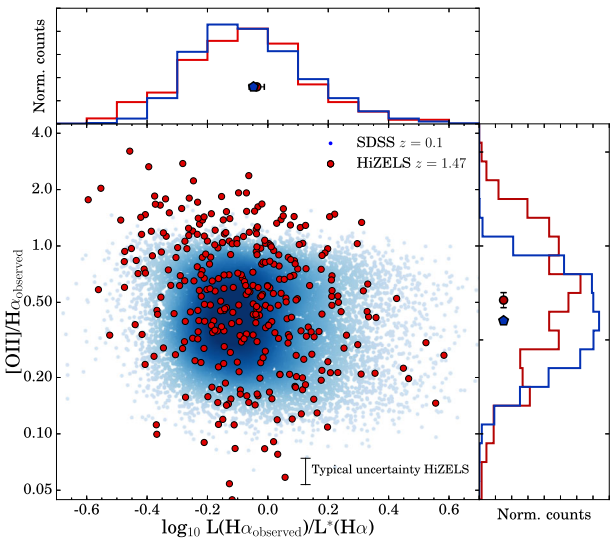

Figure 7. Observed [O II]/Hα ratio as a function of observed Hα luminosity, normalized by the typical luminosity ($L^\star$) at either $z = 1.47$ ($L^\star = 10^{42.16}$ erg s^{-1}; Sobral et al. 2013) or $z = 0.1$ ($L^\star = 10^{41.4}$ erg s^{-1}; Ly et al. 2007). The blue points (coloured by density) show the ratios observed in SDSS at $z = 0.1$, while the red points show the HiZELS measurements at $z = 1.47$. The distribution of $L/L^\star$ is similar at both redshifts, while the median observed [O II]/Hα increases from 0.40 ± 0.01 in the local Universe to 0.52 ± 0.05 at $z = 1.5$. A KS test confirms that this increase is statistically significant. This increase could be due to evolution of the dust attenuation, or an effect from fibre-measurements in SDSS.

measurements from a sample of star-forming galaxies at $z \approx 0.1$ drawn from data from SDSS DR7 (Abazajian et al. 2009) as described in Sobral et al. (2012). In short, a sample of 16 414 galaxies were selected at $0.07 < z < 0.1$ with observed Hα luminosity $>10^{40.6}$ erg s^{-1} and Hα EW >20 Å. For consistency with our sample at $z = 1.47$, we do not remove AGN using the BPT diagnostic (Baldwin, Phillips & Terlevich 1981). Aperture corrections to emission-line measurements have been done following Garn & Best (2010) based on the ratio between the stellar mass in the fibre and the total stellar mass. We note that these corrections do not change line-ratios.

In Fig. 7, we show the observed [O II]/Hα ratio as a function of observed Hα luminosity, normalized by the typical Hα luminosity ($L^\star_{\mathrm{H}\alpha}$) at the specific redshift, both for the sample of dual-emitters and the local comparison sample. After correcting for the evolution in the typical Hα luminosity of a factor of ≈6, the distribution of Hα luminosities is remarkably similar. By computing the median ratio in 100,000 bootstrap resamples of the data, we measure [O II]/H$\alpha = 0.40 \pm 0.01$ with 95 per cent confidence intervals at $z = 0.1$ (slightly lower than the measurement of 0.45 in Kennicutt 1998) and [O II]/H$\alpha = 0.55 \pm 0.07$, such that there is a slight increase of the median value with redshift (although the increase is within the observed scatter of ≈0.2–0.3 dex; see also Hayashi et al. 2013). We note that our survey may miss the galaxies with lowest [O II]/Hα ratio, in particular for the faintest Hα emitters, which may result in a bias towards finding a higher [O II]/Hα ratio at $z = 1.47$. However, if we restrict the analysis to brighter sources ($> 0.5 \times L^\star_{\mathrm{H}\alpha}$), we find [O II]/H$\alpha = 0.52 \pm 0.05$ at $z = 1.47$, while the SDSS results remain unchanged. This indicates that this selection effect is likely not driving the differences. A one-dimensional Kolmogorov-Smirnov (KS) test of the observed [O II]/Hα ratios confirms that the distributions are significantly different, with a KS-statistic of 0.20 (≈10^{-10} significance) and a P-value of 4×10^{-11}. This indicates that, even though the spread in values is relatively large (≈0.4–0.5 dex), the median observed [O II]/Hα ratio increases slightly, but statistically significantly, between $z = 0.1$–1.47.

We test whether the observed difference can be caused by systematic errors. At $z = 1.47$, there is a systematic uncertainty due to the relative filter transmissions at the different wavelengths, which leads to an increase in the scatter and a small bias towards higher [O II]/Hα values. Based on the simulation that is discussed in detail in Sobral et al. (2012), we estimate that this systematic increase is only of the order of ≈5 per cent, insufficient to explain the offset of the median ratio. If we remove AGN in the SDSS sample using the BPT criterion as defined in Kauffmann et al. (2003), we find [O II]/H$\alpha = 0.42 \pm 0.01$. Finally, if we fully mimic the Hα measurement (and its correction for the contribution of the [N II] in the narrow-band), we measure [O II]/H$\alpha = 0.45 \pm 0.01$. Thus, none of these effects can explain the observed difference, but they further highlight that the evolution is small, and thus only our large statistical sample can measure evolution.

A higher observed [O II]/Hα ratio is expected when there is less attenuation due to dust, since [O II] is attenuated more than Hα (e.g. Reddy et al. 2015). For example, it could be that galaxies at $z = 1.47$ are less dusty. Indeed, if we restrict the sample of local galaxies to those with $A_{\mathrm{H}\alpha} < 1.3$ (median $A_{\mathrm{H}\alpha} = 0.82$, compared to a median $A_{\mathrm{H}\alpha} = 0.91$ for the full sample), we find a similar observed [O II]/Hα ratio of 0.49 ± 0.01. However, results from *Herschel* stacking of Hα emitters at $z = 1.47$ (Thomson et al. 2017; see also Ibar et al. 2013) indicate that their extinction properties are similar to local galaxies, with a similar relation between stellar mass and $A_{\mathrm{H}\alpha}$ (Garn & Best 2010). We note that because the samples are matched in $L/L^\star_{\mathrm{H}\alpha}$, there are likely no significant mass differences between the samples (e.g. Sobral et al. 2014). A more detailed analysis of the extinction properties of this sample is beyond the scope of this paper. Finally, another explanation is that the SDSS fibre measurements are biased towards higher extinction (and thus lower [O II]/Hα ratios), because they measure the line-ratios in the central 3–4 kpc of galaxies, which are observed to be dustier/more evolved (e.g. Sánchez et al. 2014), while the 3 arcsec measurements at $z = 1.47$ measure flux out to radii of 8−13 kpc (depending on UDS/COSMOS or Boötes). Therefore, the observed offset between $z = 0.1$ and $z = 1.47$ could also be an observational effect due to dust, age and/or metallicity gradients within galaxy. These observational issues can be overcome with large IFU or matched NB surveys in the local Universe, as for example the J-PAS project (Benitez et al. 2014).

6.4 X-ray fraction & the power-law component of the LF

We investigate the AGN fractions of Hα emitters at $z = 1.47$ and $z = 2.23$ and LAEs at $z = 2.4$ by matching our samples to source catalogue from X-ray (*Chandra*, 0.5–7.0 keV, depth 7.8×10^{-15} erg s^{-1} cm^{-2}, 1 arcsec resolution and matching radius, Kenter et al. 2005). In addition, we include the Hα emitters at $z = 1.47$ and $z = 2.23$ in the COSMOS field from Sobral et al. (2013) and match these with the *Chandra* COSMOS point source catalogue (0.5–7.0 keV, 5.7×10^{-16} erg s^{-1} cm^{-2}; Elvis et al. 2009); see also Calhau et al. (2017) for their detailed properties. These X-ray flux limits correspond to luminosity limits of 0.3–3$\times$ 10^{44} erg s^{-1}. If such an X-ray luminosity would have its origin in star formation, it would require SFRs of $>10^{3.5-5}$ M$_\odot$ yr^{-1} (e.g. Lehmer et al. 2016), which is unlikely. This clearly indicates an AGN origin of all X-ray detections discussed in this section.

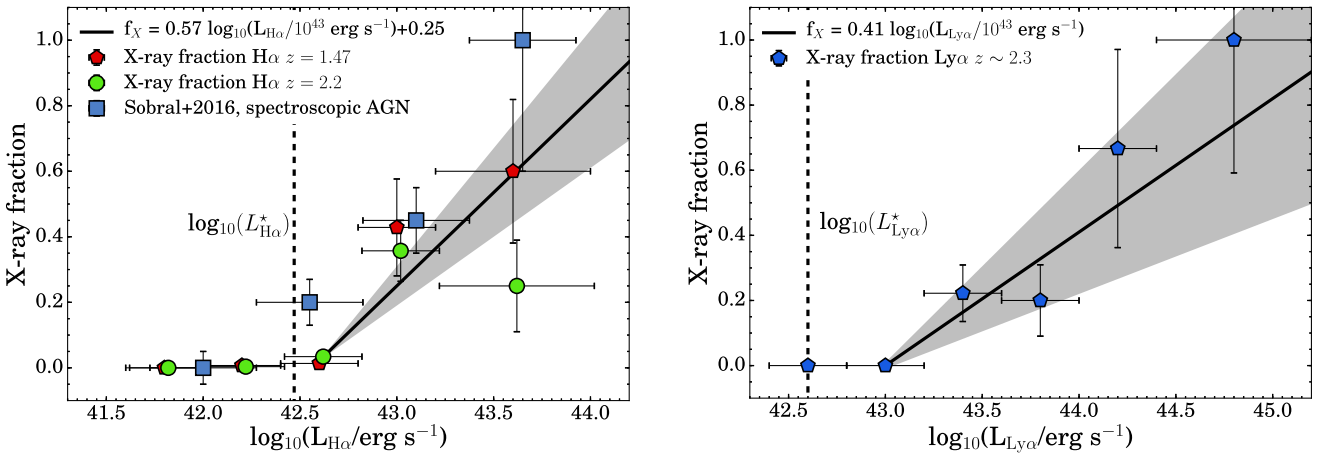

Figure 8. Left-hand panel: X-ray fraction of HAEs combining Boötes-HiZELS and the sample of emitters from COSMOS from HiZELS (Sobral et al. 2013) as a function of H α luminosity at $z = 1.47$–2.23, compared to the AGN fraction measured with spectroscopy in Sobral et al. (2016). The AGN fraction increases strongly with Hα luminosity. At fixed H α luminosity, the observed X-ray fraction does not evolve strongly between $z = 1.47$–2.23. Right-hand panel: X-ray fraction of LAEs as a function of Ly α luminosity at $z \approx 2.3$. The AGN fraction increases strongly with Ly α luminosity. The luminosities above which the X-ray fraction exceeds 20 per cent correspond to the luminosities, where the number densities start to diverge from Schechter (see e.g. Fig. 3).

In total, we detect 21 HAEs in the X-ray, of which 10 are at $z = 1.47$ and 11 are at $z = 2.23$ and half of the X-ray-detected HAEs are in Boötes. We find that the detection rate depends strongly on the H α luminosity (see Fig. 8). This has also been observed using spectroscopic follow-up by Sobral et al. (2016), who found that the majority (80 ± 30 per cent) of luminous HAEs are broad-line AGN. Relatively independent of redshift, roughly half of the most luminous HAEs are X-ray detected. Note that the other half may easily be undetected due to the short duty cycle of X-ray AGN (e.g. Shankar, Weinberg & Miralda-Escudé 2009; Fiore et al. 2012), although it could also indicate that roughly half of the luminous HAEs are optically thick to X-rays. By combining the data points above $L^\star$ at $z = 1.47$–2.23, we find a best-fitting $f_X = 0.57^{+0.15}_{-0.15}\log_{10}(L_{H\alpha}/10^{43}\ \mathrm{erg\ s^{-1}}) + 0.25^{+0.06}_{-0.06}$ that we illustrate in Fig. 8.

We combine the sample of LAEs at $z = 2.2$–2.4 identified with the NB392 and the stV filter to investigate the X-ray fraction of LAEs as a function of luminosity. Out of the 41 LAEs, eight are X-ray detected ($L_X \gtrsim 3 \times 10^{44}$ erg s^{-1}). The X-ray fraction of LAEs increases strongly with line luminosity, from ≈0 per cent at $L^\star_{Ly\alpha}$ to ≈100 per cent at $\gtrsim 3 \times 10^{44}$erg s^{-1}. We note that the Ly α luminosities at which the X-ray fraction exceeds 20 per cent correspond to the luminosities at which the number densities start to deviate from a Schechter function, as observed in Konno et al. (2016), Sobral et al. (2017) and this work (Fig. 3). For both H α and Ly α, the X-ray fraction increases above $L^\star$. For Ly α, we find a best-fitting relation of $f_X = 0.41^{+0.18}_{-0.18}\log_{10}(L_{Ly\alpha}/10^{43}\ \mathrm{erg\ s^{-1}})$ above $L_{Ly\alpha} > 10^{43}$ erg s^{-1}.

7 CONCLUSIONS

We presented the first results from the Boötes-HiZELS survey, which uses six narrow-bands to select emission-line galaxies from $z = 0.4$–4.7 in a 0.7 deg^2 region in the Boötes field. We described the observations, data-reduction, extraction of catalogues and selection of line-emitters, and how multiwavelength data has been used to classify different populations of line-emitters. The main results are:

(i) We identify 362 candidate H α emitters (HAEs) at $z = 0.4$, 1.47, 2.23, 387 H β/[O III] emitters at $z = 0.8$, 2.23, 3.3, 285 [O II] emitters at $z = 1.47$, 3.3, 4.7 and 73 Ly α emitters (LAEs) at $z = 2.23$, 2.3, 3.1.

(ii) Using a suite of matched narrow-band filters, we identify 42 galaxies with emission lines in multiple narrow-bands, providing 22/18 new robust redshift identifications of [O II]/H α and [O III]/H α emitters at $z = 1.47/2.23$, without pre-selection on AGN activity or I-band magnitude (see Section 6 and Table C1). 56 additional line-emitters have a spectroscopic redshift.

(iii) In general, the number densities of line-emitters as a function of luminosity we derive agree remarkably well with LFs observed in other survey fields (Section 5; Figs 3–5), confirming strong evolution in $L^\star_{H\alpha}$ from $z = 0.4$–2.2 and evolution in $L^\star_{Ly\alpha}$ from $z = 2.2$–3.1.

(iv) We confirm the result from Konno et al. (2016) and Sobral et al. (2017) that the LF of LAEs at $z \approx 2.2$ diverges from a Schechter function at the bright end, $L_{Ly\alpha} \gtrsim 10^{43}$ erg s^{-1}. At these luminosities, the LF follows $\log_{10}(\Phi) = 27.5 - 0.74\log_{10}(L_{Ly\alpha})$. Such a departure from a Schechter function is also clearly observed at the highest H α luminosities ($L_{H\alpha} \gtrsim 10^{43.5}$ erg s^{-1}) at $z = 2.2$ (Sections 5.2 and 5.2.2).

(v) Combining our sample of dual-emitters with those from the COSMOS and UDS fields from HiZELS, we compare the observed [O II]/H α ratio of 340 star-forming galaxies at $z = 1.47$ with those from a reference sample in the local Universe (Section 6.3). We measure a median ratio of [O II]/H $\alpha = 0.40 \pm 0.01$ at $z = 0.1$ and [O II]/H $\alpha = 0.55 \pm 0.07$ ([O II]/H $\alpha = 0.52 \pm 0.05$ if we restrict the sample to sources with slightly higher S/N, see Fig. 7). The ≈0.1 dex offset can potentially be attributed to a lower dust attenuation at $z = 1.47$, or biases in the fibre-measurements in the local Universe, which measure the ratio at the central 3–4 kpc of galaxies, while the measurements at $z = 1.47$ are integrated over ≈10kpc.

(vi) By exploiting *Chandra* X-ray data, we show that the H α and Ly α luminosities at which the number densities start to diverge from pure Schechter form at similar luminosities to where the X-ray fractions start to increase, from 20 to ∼100 per cent (Fig. 8). We also show that, under basic assumptions, the majority of luminous LAEs are not broad-line Type I AGN (Fig. 3), and more likely narrow-line Type II AGN.

The sample of identified line-emitters can be used to study various properties of star-forming galaxies. In particular, the

relatively large sample of Hα emitters at $z = 1.5$–2.2 can be used to test various SFR indicators (Hα, rest-UV, radio, FIR) in future papers.

ACKNOWLEDGEMENTS

We thank the referee for their constructive comments which helped improve the quality of this work. JM acknowledges the support of a Huygens PhD fellowship from Leiden University and JM and DS acknowledge financial support from a NWO/VENI grant awarded to David Sobral. IRS acknowledges support from STFC (ST/L00075X/1), the ERC Advanced Grant DUSTYGAL (321334) and a Royal Society/Wolfson Merit Award. HR acknowledges support from the ERC Advanced Investigator programme New-Clusters 321271. PNB is grateful to STFC for support via grant ST/M001229/1. BD acknowledges financial support from NASA through the Astrophysics Data Analysis Program (ADAP), grant number NNX12AE20G. We thank Ana Afonso, João Calhau, Leah Morabito, Iván Oteo, Sérgio Santos and Aayush Saxena for their assistance with observations. This work is based on observations obtained using the Wide Field Camera (WFCAM) on the 3.8-m United Kingdom Infrared Telescope (UKIRT), as part of the High-redshift(Z) Emission-Line Survey (HiZELS; U/CMP/3 and U/10B/07), using Suprime-Cam on the 8.2-m Subaru Telescope as part of programme S14A-086 and using the WFC on the 2.5-m Isaac Newton Telescope, as part of programmes 2013AN002, 2013BN008, 2014AC88, 2014AN002, 2014BN006, 2014BC118 and 2016AN001, using ISIS and AF2+WYFFOS on the 4.2-m William Herschel Telescope, as part of programmes 2016AN004 and 2016BN011 and using DEIMOS on the 10-m Keck II Telescope as part of programme C267D and on observations made with ESO Telescopes at the La Silla Paranal Observatory under ESO programme IDs 098.A-0819 and 179.A-2005. This work made use of images and/or data products provided by the NOAO Deep Wide-Field Survey (Jannuzi & Dey 1999) which is supported by the National Optical Astronomy Observatory (NOAO). NOAO is operated by AURA, Inc., under a cooperative agreement with the National Science Foundation. We have benefited greatly from the public available programming language PYTHON, including the NUMPY, MATPLOTLIB, PYFITS, SCIPY and ASTROPY packages (Astropy Collaboration et al. 2013), the astronomical imaging tools SEXTRACTOR, SWARP and SCAMP and the TOPCAT analysis program (Taylor 2013).

REFERENCES

Abazajian K. N. et al., 2009, ApJS, 182, 543
Alexandroff R. et al., 2013, MNRAS, 435, 3306
An F., Zheng X., HAO C.-N., Huang J.-S., Xia X.-Y., 2016, 835, 116
Ashby M. L. N. et al., 2009, ApJ, 701, 428
Astropy Collaboration et al., 2013, AAP, 558, A33
Baldwin J. A., Phillips M. M., Terlevich R., 1981, PASP, 93, 5
Beare R., Brown M. J. I., Pimbblet K., Bian F., Lin Y.-T., 2015, ApJ, 815, 94
Benitez N. et al., 2014, preprint (arXiv:1403.5237)
Bertin E., 2006, in Gabriel C., Arviset C., Ponz D., Enrique S., eds, ASP Conf. Ser. Vol. 351, Astronomical Data Analysis Software and Systems XV. Astron. Soc. Pac., San Francisco, p. 112
Bertin E., 2010, SWarp: Resampling and Co-adding FITS Images Together, Astrophysics Source Code Library (ascl:1010.068)
Bertin E., Arnouts S., 1996, AAPS, 117, 393
Best P. et al., 2013, in Adamson A., Davies J., Robson I., eds, Astrophysics and Space Science Proc. Vol. 37, Thirty Years of Astronomical Discovery with UKIRT. Springer Science+Business Media, Dordrecht, Netherlands, p. 235
Bian F. et al., 2012, ApJ, 757, 139
Bian F. et al., 2013, ApJ, 774, 28
Bongiorno A. et al., 2007, AAP, 472, 443
Bongiorno A. et al., 2010, AAP, 510, A56
Bunker A. J., Warren S. J., Hewett P. C., Clements D. L., 1995, MNRAS, 273, 513
Calhau J., Sobral D., Stroe A., Best P., Smail I., Lehmer B., Harrison C., Thomson A., 2017, MNRAS, 464, 303
Colbert J. W. et al., 2013, ApJ, 779, 34
Daddi E., Cimatti A., Renzini A., Fontana A., Mignoli M., Pozzetti L., Tozzi P., Zamorani G., 2004, ApJ, 617, 746
Dawson S., Rhoads J. E., Malhotra S., Stern D., Wang J., Dey A., Spinrad H., Jannuzi B. T., 2007, ApJ, 671, 1227
Dey A., Lee K.-S., Reddy N., Cooper M., Inami H., Hong S., Gonzalez A. H., Jannuzi B. T., 2016, ApJ, 823, 11
Drake A. B. et al., 2013, MNRAS, 433, 796
Elvis M. et al., 2009, ApJS, 184, 158
Fiore F. et al., 2012, AAP, 537, A16
Fumagalli M. et al., 2012, ApJ, 757, L22
Garn T., Best P. N., 2010, MNRAS, 409, 421
Garn T. et al., 2010, MNRAS, 402, 2017
Geach J. E., Smail I., Best P. N., Kurk J., Casali M., Ivison R. J., Coppin K., 2008, MNRAS, 388, 1473
Gonzalez A. H. et al., 2010, in American Astronomical Society Meeting Abstracts #216, p. 415.13
Hayashi M., Sobral D., Best P. N., Smail I., Kodama T., 2013, MNRAS, 430, 1042
Hayes M., 2015, PASA, 32, e027
Hildebrandt H., Pielorz J., Erben T., van Waerbeke L., Simon P., Capak P., 2009, AAP, 498, 725
Hunt M. P., Steidel C. C., Adelberger K. L., Shapley A. E., 2004, ApJ, 605, 625
Ibar E. et al., 2013, MNRAS, 434, 3218
Jannuzi B. T., Dey A., 1999, in Weymann R., Storrie-Lombardi L., Sawicki M., Brunner R., eds, ASP Conf. Ser. Vol. 191, Photometric Redshifts and the Detection of High Redshift Galaxies. Astron. Soc. Pac., San Francisco, p. 111
Jansen R. A., Franx M., Fabricant D., 2001, ApJ, 551, 825
Kauffmann G. et al., 2003, MNRAS, 346, 1055
Kennicutt R. C., Jr, 1998, ARAA, 36, 189
Kenter A. et al., 2005, ApJS, 161, 9
Khostovan A. A., Sobral D., Mobasher B., Best P. N., Smail I., Stott J. P., Hemmati S., Nayyeri H., 2015, MNRAS, 452, 3948
Khostovan A. A., Sobral D., Mobasher B., Smail I., Darvish B., Nayyeri H., Hemmati S., Stott J. P., 2016, MNRAS, 463, 2363
Kochanek C. S. et al., 2012, ApJS, 200, 8
Konno A., Ouchi M., Nakajima K., Duval F., Kusakabe H., Ono Y., Shimasaku K., 2016, ApJ, 823, 20
La Franca F. et al., 2005, ApJ, 635, 864
Laigle C. et al., 2016, ApJS, 224, 24
Lee J. C. et al., 2012, PASP, 124, 782
Lee K.-S. et al., 2011, ApJ, 733, 99
Lee K.-S., Dey A., Hong S., Reddy N., Wilson C., Jannuzi B. T., Inami H., Gonzalez A. H., 2014, ApJ, 796, 126
Lehmer B. D. et al., 2016, ApJ, 825, 7
Ly C. et al., 2007, ApJ, 657, 738
Ly C., Malkan M. A., Kashikawa N., Hayashi M., Nagao T., Shimasaku K., Ota K., Ross N. R., 2012, ApJ, 757, 63
Malkan M. A., Teplitz H., McLean I. S., 1996, ApJ, 468, L9
Martin D. C. et al., 2005, ApJ, 619, L1
Matsuda Y. et al., 2004, AJ, 128, 569
Matthee J. J. A. et al., 2014, MNRAS, 440, 2375
Matthee J., Sobral D., Santos S., Röttgering H., Darvish B., Mobasher B., 2015, MNRAS, 451, 400
Matthee J., Sobral D., Oteo I., Best P., Smail I., Röttgering H., Paulino-Afonso A., 2016, MNRAS, 458, 449

Murray S. S. et al., 2005, ApJS, 161, 1
Muzzin A. et al., 2013, ApJS, 206, 8
Nakajima K. et al., 2012, ApJ, 745, 12
Oliver S. J. et al., 2012, MNRAS, 424, 1614
Oteo I., Sobral D., Ivison R. J., Smail I., Best P. N., Cepa J., Pérez-García A. M., 2015, MNRAS, 452, 2018
Ouchi M. et al., 2004, ApJ, 611, 660
Ouchi M. et al., 2008, ApJs, 176, 301
Prescott M. K. M., Kashikawa N., Dey A., Matsuda Y., 2008, ApJL, 678, L77
Reddy N. A. et al., 2015, ApJ, 806, 259
Rhoads J. E., Malhotra S., Dey A., Stern D., Spinrad H., Jannuzi B. T., 2000, ApJ, 545, L85
Sánchez S. F. et al., 2014, AAP, 563, A49
Santos S., Sobral D., Matthee J., 2016, MNRAS,
Schechter P., 1976, ApJ, 203, 297
Shankar F., Weinberg D. H., Miralda-Escudé J., 2009, ApJ, 690, 20
Skrutskie M. F. et al., 2006, AJ, 131, 1163
Sobral D. et al., 2009, MNRAS, 398, 75
Sobral D., Best P. N., Matsuda Y., Smail I., Geach J. E., Cirasuolo M., 2012, MNRAS, 420, 1926
Sobral D., Smail I., Best P. N., Geach J. E., Matsuda Y., Stott J. P., Cirasuolo M., Kurk J., 2013, MNRAS, 428, 1128
Sobral D., Best P. N., Smail I., Mobasher B., Stott J., Nisbet D., 2014, MNRAS, 437, 3516
Sobral D. et al., 2015, MNRAS, 451, 2303
Sobral D., Kohn S. A., Best P. N., Smail I., Harrison C. M., Stott J., Calhau J., Matthee J., 2016, MNRAS, 457, 1739
Sobral D. et al., 2017, MNRAS, 466, 1242
Speagle J. S., Steinhardt C. L., Capak P. L., Silverman J. D., 2014, ApJS, 214, 15
Stott J. P. et al., 2013, MNRAS, 436, 1130
Stroe A., Sobral D., 2015, MNRAS, 453, 242
Stroe A., Sobral D., Röttgering H. J. A., van Weeren R. J., 2014, MNRAS, 438, 1377
Stroe A., Sobral D., Matthee J., Calhau J., Oteo I., 2017, MNRAS, preprint (arXiv:1703.10169)
Tadaki K.-I., Kodama T., Koyama Y., Hayashi M., Tanaka I., Tokoku C., 2011, PASJ, 63, 437
Taylor M., 2013, Starlink User Note, 253
Thomson A. P. et al., 2017, ApJ, 838, 119
van der Wel A. et al., 2011, ApJ, 742, 111
van der Werf P. P., Moorwood A. F. M., Bremer M. N., 2000, AAP, 362, 509
Vanden Berk D. E. et al., 2001, AJ, 122, 549
Williams W. L. et al., 2016, MNRAS, 460, 2385
Xue R. et al., 2017, ApJ, 837, 172
Yamada T., Nakamura Y., Matsuda Y., Hayashino T., Yamauchi R., Morimoto N., Kousai K., Umemura M., 2012, AJ, 143, 79

SUPPORTING INFORMATION

Supplementary data are available at *MNRAS* online.

Table C1. List of sources that are observed as dual-emitters (line-emitters in at least two narrow-bands).
Table D1. First five entries in the catalogue of NB392 line-emitters.
Table D2. First five entries in the catalogue of stV line-emitters.
Table D3. First five entries in the catalogue of NB501 line-emitters.
Table D4. First five entries in the catalogue of NB921 line-emitters.
Table D5. First five entries in the catalogue of NB_H line-emitters.
Table D6. First five entries in the catalogue of NB_K line-emitters.

Please note: Oxford University Press is not responsible for the content or functionality of any supporting materials supplied by the authors. Any queries (other than missing material) should be directed to the corresponding author for the article.

APPENDIX A: PHOTOMETRIC CONSISTENCY CHECK

In our catalogue production steps (Section 3.2), we only include objects in our catalogues that have a physically plausible NB excess. Because the BB covers the same wavelength as the NB, flux in the NB must also be observed in the BB, otherwise the object is either unreal (such as a cosmic ray and artefacts) or variable (such as variable stars, supernovae or AGN). It is fairly straightforward to compute the faintest possible BB magnitude, given an NB magnitude:

$$\mathrm{BB_{max}} = \mathrm{NB} - 2.5\log_{10}\left(\frac{\lambda^2_{\mathrm{c,BB}}\Delta\lambda_{\mathrm{NB}}}{\lambda^2_{\mathrm{c,NB}}\Delta\lambda_{\mathrm{BB}}}\right) + 0.5, \quad \text{(A1)}$$

where $\lambda_{\mathrm{c,X}}$ is the central wavelength of filter X and $\Delta\lambda_{\mathrm{X}}$ is the width of filter X. We conservatively add 0.5 magnitude to take into account uncertainties in the photometry and relative filter transmissions. We remove any source for which the excess is larger than $\mathrm{BB_{max}} - \mathrm{NB}$. For example, for NB921 and z band, this equation results in $\mathrm{BB_{max}} = \mathrm{NB} + 3.4$. This means that if a source has a NB921 magnitude of 20, it must have a z magnitude of 23.4 or brighter. It is possible that the implied $\mathrm{BB_{max}}$ is below the background. In that case, we exclude sources for which the BB is not detected at 2σ. This consistency check removes most spurious objects such as cosmic rays and detector artefacts.

APPENDIX B: COLOUR–COLOUR SELECTIONS

In this section, we illustrate the colour–colour selection criteria outlined in Table 3. In all figures (Figs B1–B5), line-emitters with secure redshift identifications from spectroscopy or dual-NB detections are shown with larger symbols. X-ray-detected AGN are shown with a star symbol.

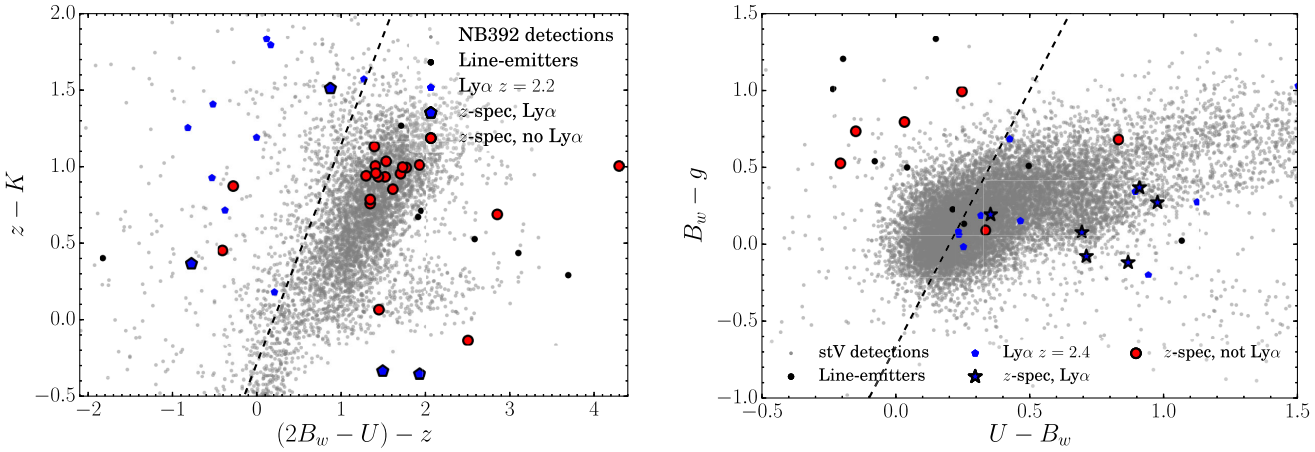

Figure B1. Colour selection criteria used to select LAEs at $z = 2.2$ and $z = 2.4$. These are based on the BzK criterion from Daddi et al. (2004). The B_w band magnitude is adjusted for the contribution to flux in the U band. We highlight the sources with spectroscopic redshifts in larger symbols.

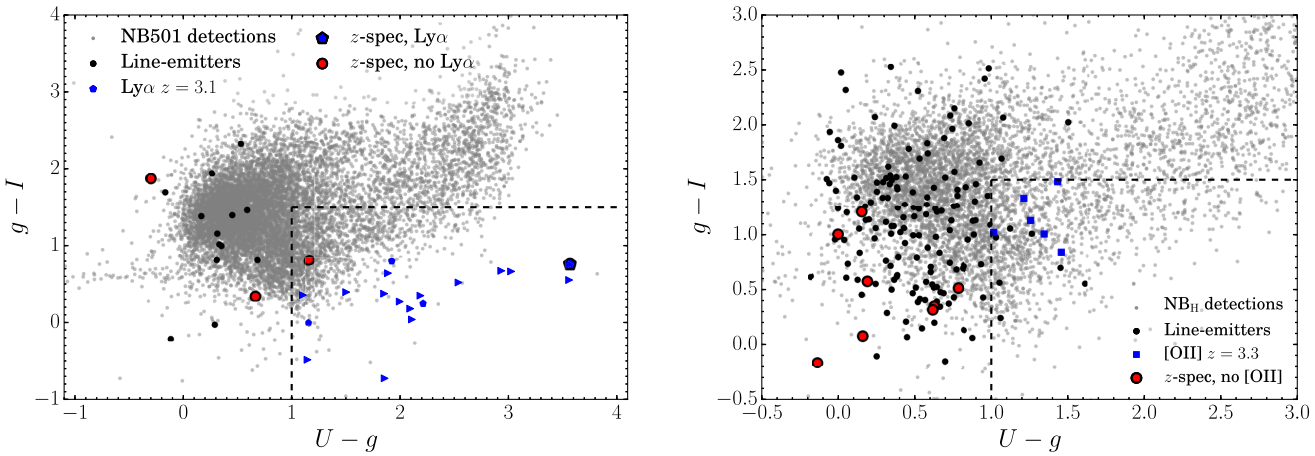

Figure B2. Colour selection criterion used to select LAEs at $z = 3.1$ (from NB501) and [O III]/Hβ at $z = 3.2$ (from NB_H), based on the U drop-out criterion for Lyman-break galaxies at $z \approx 3$ from Hildebrandt et al. (2009). The $U - g$ colour identifies the Lyman break, while the $g - I$ criterion removes any sources for which the Balmer break is mimicked by a strong Balmer break (particularly important in the case a galaxy is very dusty).

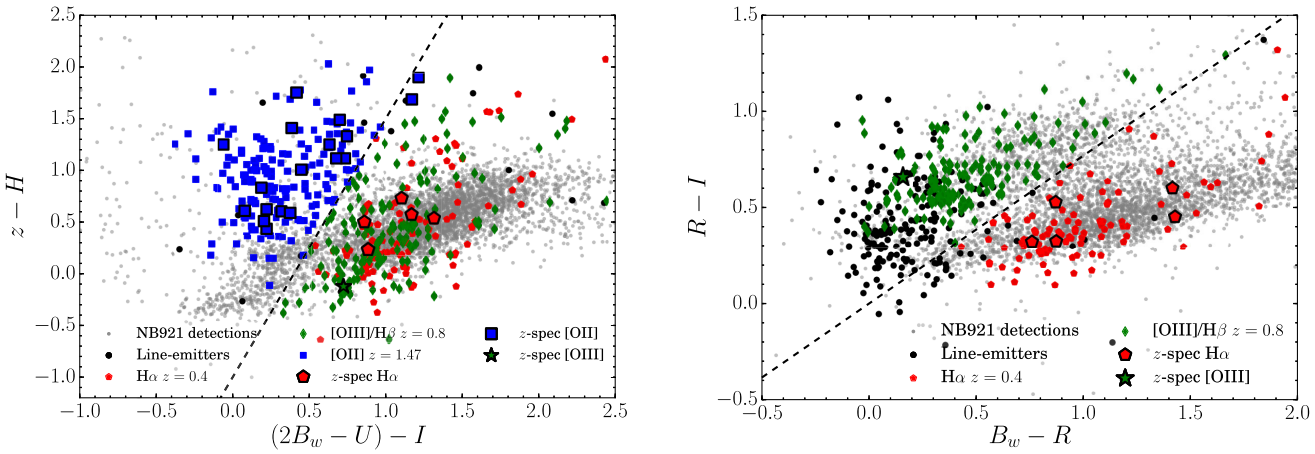

Figure B3. Colour selection criteria used to distinguish Hα, [O III]/Hβ and [O II] emitters amongst the line-emitters identified with NB921. The criterion in the left-hand panel identifies Balmer breaks at specific redshift intervals. Because this criterion cannot distinguish between $z = 0.4$ and $z = 0.8$, we use the additional B_wRI colours to distinguish between a Balmer break between B_w and R (around 600 nm, or $z \approx 0.5$) and between R and I (around 700 nm, or $z \approx 0.75$).

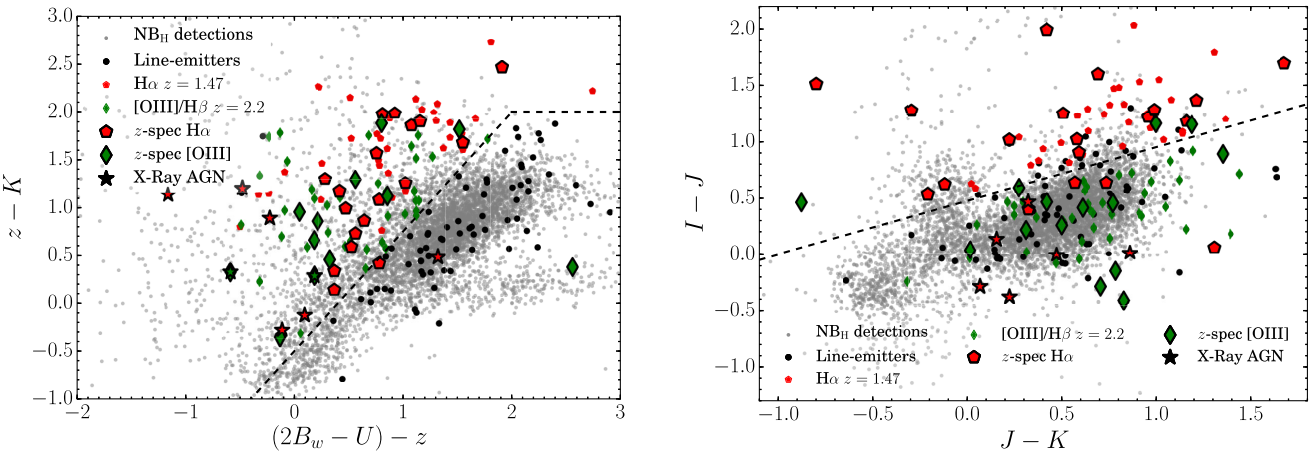

Figure B4. Colour criteria used to classify line-emitters identified with the NB$_H$ filter. The modified B_wzK criterion is used to distinguish $z > 1$ line-emitters from $z < 1$ line-emitters. We then distinguish between $z = 1.47$ and $z = 2.2$ based on the positions of Balmer breaks. At $z \approx 1.5$, the Balmer break lies around an observed 1000 nm, hence between $I - J$ (note that we use I rather than z because I is deeper and broader, see Table 1). At $z \approx 2.2$, the Balmer break lies between the J and K bands. Note that several X-ray-detected Hα emitters at $z = 1.47$ mimic the colours of $z = 2.2$ [O III]/Hβ emitters. These sources typically have high line-fluxes and their spectroscopic follow-up completeness is high. [O II] emitters at $z = 3.3$ are selected based on the position of their Lyman-break, similar to LAEs at $z = 3.1$ in Fig. B2.

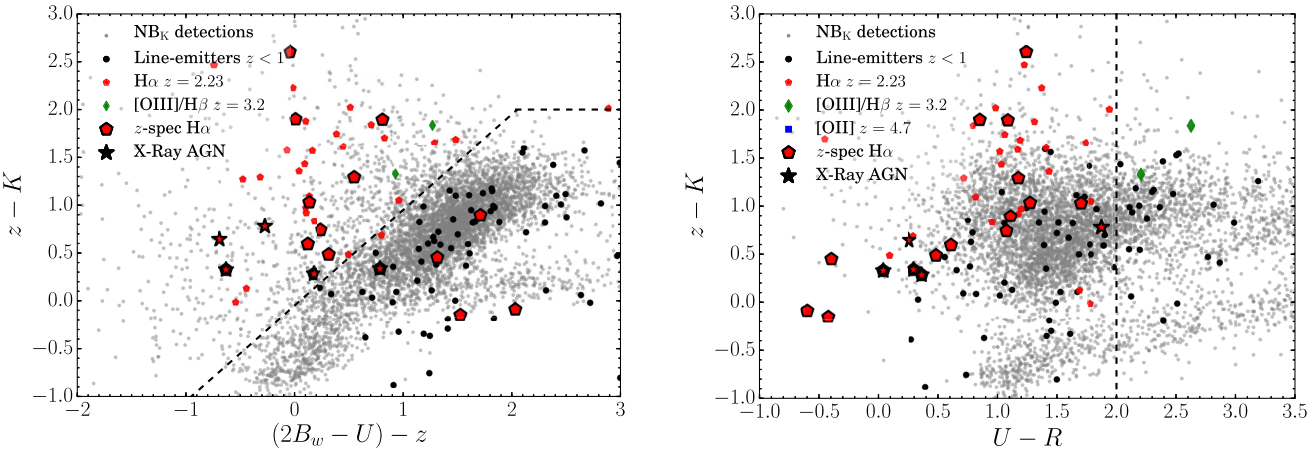

Figure B5. Colour criteria used to classify line-emitters identified with the NB$_K$ filter. Similarly to the line-emitters in the NB$_H$ filter, we use the modified B_wzK criterion to selected line-emitters at $z > 1$ (left-hand panel). We then distinguish those between Hα at $z = 2.23$ and [O III]/Hβ emitters at $z = 3.2$ based on the positions of their Lyman breaks.

APPENDIX C: CATALOGUE OF DUAL-EMITTERS

Table C1. List of sources that are observed as dual-emitters (line-emitters in at least two narrow-bands). We present the coordinates, spectroscopic and dual-NB redshifts, I-band magnitudes and the list of emission lines that are detected. X-ray- and LOFAR-detected sources are marked. We note that because the coverage in NB392, stV and NB921 is not homogeneous, the number of Lyα detections at $z = 2.23$ and [O II] at $z = 1.47$ is likely underestimated. An electronic version of this table is available online.

ID	RA	Dec.	$z_{\rm dual\text{-}NB}$	$z_{\rm spec}$	I	Note
B-HiZELS_1	14:33:19.29	+33:34:31.53	2.23	2.23	18.9	Lyα+[O III] + Hα
B-HiZELS_2	14:32:58.85	+33:25:49.33	2.23		19.6	Hα + Lyα + N v, X-ray detected
B-HiZELS_3	14:31:41.51	+33:49:11.27	2.23	2.26	20.4	[O III] + Hα + C IV +Lyα, X-ray detected
B-HiZELS_4	14:29:40.05	+33:33:32.13	2.23	2.27	20.6	[O III] + Hα + Mg II, X-ray detected
B-HiZELS_5	14:32:01.52	+33:16:59.86	2.23		20.9	[O III] + Hα
B-HiZELS_6	14:30:38.29	+33:20:17.85	2.23		21.3	[O III]+Hα, X-ray detected
B-HiZELS_7	14:29:30.87	+34:05:44.85	2.23		21.7	[O III]+Hα
B-HiZELS_8	14:32:13.88	+33:25:57.48	2.23		21.9	[O III] + Hα + Lyα, LOFAR detected
B-HiZELS_9	14:31:06.64	+33:46:19.18	2.23		22.1	[O III] + Hα

Table C1 – *continued*

ID	RA	Dec.	$z_{\rm dual\text{-}NB}$	$z_{\rm spec}$	I	Note
B-HiZELS_10	14:33:07.48	+33:52:42.48	1.47		22.1	[O II] + Hα
B-HiZELS_11	14:32:37.05	+33:33:56.18	1.47		22.1	[O II] + Hα
B-HiZELS_12	14:30:51.00	+33:43:54.56	2.23		22.3	[O III]+Hα
B-HiZELS_13	14:33:14.40	+33:46:53.17	1.47		22.4	[O II] + Hα
B-HiZELS_14	14:32:12.54	+33:22:26.15	1.47		22.4	[O II] + Hα
B-HiZELS_15	14:32:32.59	+33:59:03.32	2.23	2.24	22.5	[O III] + Hα + C IV, X-ray & LOFAR detected
B-HiZELS_16	14:30:40.31	+34:03:20.64	2.23		22.8	Lyα, C IV and Hα
B-HiZELS_17	14:31:33.54	+34:02:48.52	2.23		22.8	[O III] + Hα
B-HiZELS_18	14:32:52.90	+33:39:43.29	1.47		22.8	[O II] + Hα
B-HiZELS_19	14:30:16.12	+33:17:09.56	1.47		23.0	[O II] + Hα
B-HiZELS_20	14:30:28.28	+33:38:16.75	1.47		23.0	[O II] + Hα
B-HiZELS_21	14:30:19.38	+33:37:10.18	1.47		23.1	[O II] + Hα
B-HiZELS_22	14:33:15.16	+33:50:09.62	1.47		23.1	[O II] + Hα
B-HiZELS_23	14:32:37.05	+33:33:06.64	1.47		23.1	[O II] + Hα, LOFAR detected
B-HiZELS_24	14:30:12.20	+33:51:57.33	2.23		23.3	[O III] + Hα
B-HiZELS_25	14:30:26.29	+33:28:51.17	2.23		23.3	[O III] + Hα
B-HiZELS_26	14:30:39.53	+33:57:09.60	1.47		23.3	[O II] + Hα
B-HiZELS_27	14:33:19.61	+33:34:36.66	2.23		23.4	[O III] + Hα
B-HiZELS_28	14:31:50.68	+33:18:44.15	1.47		23.4	[O II] + Hα
B-HiZELS_29	14:30:28.56	+33:33:29.07	2.23		23.5	Lyα and Hα
B-HiZELS_30	14:30:54.03	+33:33:01.26	1.47		23.5	[O II] + Hα
B-HiZELS_31	14:31:19.33	+33:26:14.90	1.47		23.5	[O II] + Hα
B-HiZELS_32	14:32:48.04	+33:57:18.93	2.23		23.8	[O III] + Hα
B-HiZELS_33	14:30:45.55	+33:23:50.12	1.47		23.8	[O II] + Hα
B-HiZELS_34	14:30:29.53	+33:20:49.91	1.47		23.8	[O II] + Hα
B-HiZELS_35	14:30:18.58	+34:03:24.88	2.23		23.9	[O III] + Lyα
B-HiZELS_36	14:31:11.70	+33:41:28.69	1.47		24.0	[O II] + Hα
B-HiZELS_37	14:33:21.85	+33:54:50.65	1.47		24.2	[O II] + Hα
B-HiZELS_38	14:33:22.55	+33:48:04.57	1.47		24.3	[O II] + Hα
B-HiZELS_39	14:29:44.27	+33:50:43.84	1.47		24.3	[O II] + Hα
B-HiZELS_40	14:31:57.69	+33:16:37.87	2.23		24.9	[O II]+Hα
B-HiZELS_41	14:32:41.50	+33:26:18.45	2.23		25.5	[O III] + Hα
B-HiZELS_42	14:30:39.05	+33:51:51.16	2.23		25.8	[O III]+Hα

APPENDIX D: EXAMPLE CATALOGUES OF LINE-EMITTERS

Table D1. First five entries in the catalogue of NB392 line-emitters. Coordinates are in J2000. Line-flux is in 10^{-16} erg s^{-1} cm^{-2}. EW$_{\rm obs}$ is in Å, where −99 entries mark sources without secure continuum measurement, and have EW$_{\rm obs}$ > 550 Å. Entries with 99 are undetected in I band. Flag_Class: 0: unclassed, 1: LAE at $z = 2.2$. A full version of this table is available online.

ID	RA	Dec.	Line-flux	EW$_{\rm obs}$	I	Flag_Class
B-HiZELS_NB392_1	217.945	33.310	1.3	136	22.2	0
B-HiZELS_NB392_2	218.017	33.316	1.9	119	20.1	0
B-HiZELS_NB392_3	217.779	33.340	1.2	158	23.6	1
B-HiZELS_NB392_4	218.056	33.366	2.1	−99	99	0
B-HiZELS_NB392_5	217.675	33.386	4.2	56	21.9	0

Table D2. First five entries in the catalogue of stV line-emitters. Coordinates are in J2000. Line-flux is in 10^{-16} erg s^{-1} cm^{-2}. EW$_{\rm obs}$ is in Å, where −99 entries mark sources without secure continuum measurement, and have EW$_{\rm obs}$ > 2500 Å. Entries with 99 are undetected in I band. Flag_Class: 0: unclassed, 1: LAE at $z = 2.4$. A full version of this table is available online.

ID	RA	Dec.	Line-flux	EW$_{\rm obs}$	I	Flag_Class
B-HiZELS_stV_1	218.239	33.305	64.3	97	17.2	0
B-HiZELS_stV_2	218.021	33.314	13.9	1131	22.6	0
B-HiZELS_stV_3	217.909	33.351	13.5	590	22.5	0
B-HiZELS_stV_4	218.053	33.354	6.4	207	22.3	0
B-HiZELS_stV_5	218.086	33.353	25.7	1079	21.7	1

Table D3. First five entries in the catalogue of NB501 line-emitters. Coordinates are in J2000. Line-flux is in 10^{-16} erg s^{-1} cm^{-2}. EW_{obs} is in Å, where −99 entries mark sources without secure continuum measurement, and have $EW_{obs} > 550$ Å. Entries with 99 are undetected in *I* band. Flag_Class: 0: unclassed, 1: LAE at $z = 3.1$. A full version of this table is available online.

ID	RA	Dec.	Line-flux	EW_{obs}	*I*	Flag_Class
B-HiZELS_NB501_1	217.635	33.366	14.9	198	19.9	0
B-HiZELS_NB501_2	217.923	33.820	13.7	64	20.4	0
B-HiZELS_NB501_3	217.619	33.558	7.8	391	23.3	0
B-HiZELS_NB501_4	218.127	33.666	7.2	−99	22.9	1
B-HiZELS_NB501_5	217.668	34.056	5.4	138	22.6	0

Table D4. First five entries in the catalogue of NB921 line-emitters. Coordinates are in J2000. Line-flux is in 10^{-16} erg s^{-1} cm^{-2}. EW_{obs} is in Å, where −99 entries mark sources without secure continuum measurement, and have $EW_{obs} > 1100$ Å. Entries with 99 are undetected in *I* band. Flag_Class: 0: unclassed, 1: Hα at $z = 0.4$, 2: Hβ/[O III] at $z = 0.8$, 3: [O II] at $z = 1.47$. A full version of this table is available online.

ID	RA	Dec.	Line-flux	EW_{obs}	*I*	Flag_Class
B-HiZELS_NB921_1	217.417	33.559	3.9	40	20.5	0
B-HiZELS_NB921_2	217.990	33.277	0.3	142	24.6	0
B-HiZELS_NB921_3	217.831	33.437	0.3	59	23.7	3
B-HiZELS_NB921_4	218.220	33.662	1.3	101	22.8	3
B-HiZELS_NB921_5	217.799	33.691	0.3	70	23.9	3

Table D5. First five entries in the catalogue of NB_H line-emitters. Coordinates are in J2000. Line-flux is in 10^{-16} erg s^{-1} cm^{-2}. EW_{obs} is in Å, where −99 entries mark sources without secure continuum measurement, and have $EW_{obs} > 1200$ Å. Entries with 99 are undetected in *I* band. Flag_Class: 0: unclassed, 1: Hα at $z = 1.47$, 2: Hβ/[O III] at $z = 2.2$, 3: [O II] at $z = 3.3$. A full version of this table is available online.

ID	RA	Dec.	Line-flux	EW_{obs}	*I*	Flag_Class
B-HiZELS_NBH_1	218.345	33.265	1.7	188	99	0
B-HiZELS_NBH_2	218.329	33.299	2.1	212	99	0
B-HiZELS_NBH_3	217.990	33.312	1.8	474	25.5	0
B-HiZELS_NBH_4	218.165	33.317	1.8	139	22.1	0
B-HiZELS_NBH_5	217.670	33.344	1.6	180	22.8	0

Table D6. First five entries in the catalogue of NB_K line-emitters. Coordinates are in J2000. Line-flux is in 10^{-16} erg s^{-1} cm^{-2}. EW_{obs} is in Å, where −99 entries mark sources without secure continuum measurement, and have $EW_{obs} > 1250$ Å. Entries with 99 are undetected in *I* band. Flag_Class: 0: unclassed, 1: Hα at $z = 2.23$, 2: Hβ/[O III] at $z = 3.2$, 3: [O II] at $z = 4.7$, 4: $z < 1$. A full version of this table is available online.

ID	R.A.	Dec.	Line-flux	EW_{obs}	*I*	Flag_Class
B-HiZELS_NBK_1	218.080	33.261	0.8	121	22.3	4
B-HiZELS_NBK_2	218.345	33.265	1.1	−99	99	0
B-HiZELS_NBK_3	217.878	33.276	0.7	410	25.4	0
B-HiZELS_NBK_4	217.991	33.277	1.0	494	25.1	1
B-HiZELS_NBK_5	217.996	33.280	1.0	−99	24.8	1

This paper has been typeset from a TEX/LATEX file prepared by the author.